International Journal of Solids and Structures 270 (2023) 112179

Contents lists available at ScienceDirect

International Journal of Solids and Structures

journal homepage: www.elsevier.com/locate/ijsolstr

A Cartesian spatial discretization method for nonlinear dynamic modeling and vibration analysis of tensegrity structures

Sichen Yuan [a,*], Weidong Zhu [b]

[a] A. Leon Linton Department of Mechanical, Robotics and Industrial Engineering, Lawrence Technological University, Southfield, MI 48075, the United States of America
[b] Department of Mechanical Engineering, University of Maryland, Baltimore County, Baltimore, MD 21250, the United States of America

ARTICLE INFO

Keywords:
Tensegrity structure
Nonlinear dynamic modeling
Vibration analysis
Spatial discretization method
Linearized tensegrity dynamics
Lagrangian method

ABSTRACT

For vibration analysis of a tensegrity structure, the development of a dynamic model is a key step. A common issue in the traditional dynamic modeling methods for vibration analysis of tensegrity structures is that structural members are oversimplified. Member internal displacements, including those in longitudinal directions for bar and cable members and those in transverse directions for cable members, were neglected. This oversimplification would inevitably prevent the dynamic model of a tensegrity structure so developed from revealing accurate responses, especially for those in the high-frequency domain. To resolve this issue, a new method called the Cartesian spatial discretization method is developed for nonlinear dynamic modeling and vibration analysis of tensegrity structures. This method can successfully incorporate member internal displacements in dynamic modeling of a tensegrity structure by defining positions of structural members as a summation of internal terms and boundary-induced terms in a global Cartesian coordinate system. The proposed method is applied to vibration analysis of a planar Snelson's X tensegrity structure, a three-dimensional tensegrity tower, and an irregular tensegrity grid in simulation, and compared with the Lagrangian method based on generalized coordinates, the commercial finite element analysis software ANSYS and the finite element analysis method in literatures, respectively. Results show that the proposed method is accurate in predicting dynamic responses of tensegrity structures, especially for vibration analysis in the high-frequency domain. It is also demonstrated that the proposed method is applicable to both simple and complex tensegrity structures, and computationally efficient as it converges in a super-linear rate by using only a small number of internal terms of member displacements.

1. Introduction

Tensegrity structures, due to their lightweight, foldability and high stiffness, have experienced continued research and development interests in the past several decades. Due to the capability of sustaining large deformations, tensegrity structures are recognized as flexible or deployable structures in various engineering applications, such as bridges (Rhode-Barbarigos et al., 2010; Veuve et al., 2015), space reflectors (Tibert and Pellegrino, 2002), soft robots (Caluwaerts et al., 2014; Shah et al., 2021; Yuan et al., 2021), mechanical metamaterials (De Tommasi et al., 2017; Liu et al., 2019), and active building façades that harvest wind and solar energy (Cimmino et al., 2017). Tensegrity structures have also been popular for mechanical modeling of cell structures (Ingber, 2003) in biology. As an engineering structural design concept, a tensegrity structure was first introduced by Fuller (1982). In this early work, a tensegrity structure is defined as a pin-jointed structure that is composed of isolated members in compression (usually bars or struts) inside a net of continuous members in tension (usually cables or tendons). A tensegrity structure is designed so that its compressed members do not touch each other and prestressed tensioned members spatially delineate the structure. This definition was later generalized by Motro (1996), where a tensegrity structure consists of both bars and cables, with contacts among bar members being allowed.

In existing work of design and analysis, tensegrity structures are investigated mainly from a static point of view. Design of a tensegrity structure usually starts from topology design. Then an initial equilibrium configuration of the structure is obtained by a procedure named form finding, where the geometric configuration and force distribution among members of the structure are determined (Schek, 1974; Yuan and Yang, 2019; Zhang and Ohsaki, 2006). For tensegrity structures with

* Corresponding author.
E-mail address: syuan@ltu.edu (S. Yuan).

https://doi.org/10.1016/j.ijsolstr.2023.112179
Received 7 September 2022; Received in revised form 5 January 2023; Accepted 20 February 2023
Available online 24 February 2023

high surface accuracy requirements and multiple states of self-stress, self-stress determination, which is also called member force assignment or force finding, is needed. If nodal positions of a tensegrity structural are restricted by high surface accuracy requirements, optimal design of its stiffness and stability can only be accomplished by assignment of member internal forces (Feng, 2017; Tran and Lee, 2010; Yuan and Zhu, 2021).

Revealing dynamic characteristics of tensegrity structures, for example, vibration and deployment analysis, is another important objective in structural design and analysis. Early research was found in work of Motro et al. (1987), who obtained dynamic responses of a tensegrity structure by both numerical and experimental approaches, and in work of Furuya (1992), who performed vibration analysis of a tensegrity mast and revealed a relationship between natural frequencies and self-stress of the structure.

For vibration analysis of a tensegrity structure, the development of a dynamic model is a key step. One commonly used type of approach for dynamic modeling of tensegrity structures is the Lagrangian method, which was seen in works of Skelton and Sultan (1997), Sultan et al. (2002a), Sultan et al. (2002b), Sultan and Skelton (2003), Oppenheim and Williams (2001a), Oppenheim and Williams (2001b) and Kan et al. (2018b). In this type of approach, a system of generalized coordinates, which is highly coupled with the topology and the geometric configuration of a specific tensegrity structure, is first defined. All generalized coordinates are required to be independent of each other. By treating bar and cable members of the tensegrity structure as rigid bodies and massless springs, respectively, a system of second-order nonlinear ordinary differential equations (ODEs) that describes the mechanical motion of the structure is obtained by the Lagrangian method. This type of methods was later modified for dynamic modeling of tensegrity-membrane systems (Yang and Sultan, 2016, 2017, 2019), in which bar members were modeled as truss elements with flexibilities along their longitudinal directions being considered. The Lagrangian method is preferred for dynamic modeling of large-scale tensegrity structures (tensegrity structures with many nodes and members). The advantage of using generalized coordinates is that design constraints, such as axial symmetry, of a tensegrity structure are well maintained.

Another approach to dynamic modeling of tensegrity structures is the finite element analysis (FEA) methods, which were seen in works of Ali et al. (2010), Ali and Smith (2010), Faroughi and Tur (2015), Ashwear and Eriksson (2014), Ashwear et al. (2016), Feng et al. (2018) and Kahla et al. (2020). This type of modeling methods starts by obtaining mass and stiffness matrices of a single member obtained in a local coordinate system. Then, mass and stiffness matrices of a whole tensegrity structure are established by transforming from local to global coordinates through a corotational approach. This type of methods provides a simple approach in obtaining a linear dynamic model for vibration analysis. However, it is inefficient when these methods are applied to tensegrity structures subjected to large displacements, such as deployment, since large rigid-body motions of structural members are not considered. Kan et al. (2018a), Peng et al. (2020) and Ma et al. (2022) directly used global coordinates in obtaining mass and stiffness matrices of each member. This method is applicable to nonlinear dynamic analysis, since large rigid-body motions are naturally handled by global coordinates.

A common issue in the traditional dynamic modeling methods for tensegrity structures is that structural members are oversimplified. Member internal displacements, including those in the longitudinal directions for bar and cable members and those in the transverse directions for cable members, were neglected. In the traditional methods, structural members were either modeled as rigid bodies and massless springs with no internal displacements at all (seen in Lagrange-based methods), or as elastic rods with an assumption of uniform distribution of internal displacements (see shape functions used by FEA-based methods). In fact, the impact of member internal displacements on dynamic characteristics of a tensegrity structure is significant, which shall be seen in numerical simulation of this work. This oversimplification would inevitably prevent the dynamic model of a tensegrity structure so developed from revealing accurate responses, especially for those in the high-frequency domain.

To fill the above-mentioned technical gap, a novel method for nonlinear dynamic modeling of tensegrity structures, named the Cartesian spatial discretization (CSD) method, is developed in this work. This method defines positions of structural members as a summation of internal terms and boundary-induced terms in a global Cartesian coordinate system. A nonlinear dynamic model of a member is then derived from Lagrange's equations as a system of ODEs. This dynamic model can be linearized at an equilibrium configuration of the tensegrity structure for vibration analysis. A dynamic model of the whole structure is finally assembled by using common nodal coordinates of structural members. The proposed method is new in that member internal displacements are well incorporated in the nonlinear dynamic model of a tensegrity structure so developed. Thus, the oversimplification of structural members, which was often seen in the traditional dynamic modeling methods, is successfully avoided. The incorporation of member internal displacements grants the proposed method an ability to predict accurate dynamic responses of tensegrity structures, especially for vibration analysis in the high-frequency domain. In addition, the use of a global Cartesian coordinate system by the proposed method in member modeling provides a fast and straight-forward structure assembly, and automatic incorporation of rigid-body motions of structural members. The proposed method is applicable to both simple and complex tensegrity structures, and computationally efficient as it converges in a super-linear rate by using only a small number of internal terms of member displacements.

The remainder of this paper is arranged as follows. Properties and relevant concepts of tensegrity structures are clarified in Section 2. The spatial discretization method for one-dimensional continuous bar and cable members is introduced in Section 3. The CSD method for nonlinear dynamic modeling of tensegrity structures is presented in Section 4. Results from numerical simulations are given in Section 5. Conclusions from this study are presented in Section 6.

2. Problem Statement, form finding and force finding

The objective of this research is to provide an approach to nonlinear dynamic modeling and vibration analysis of tensegrity structures. Properties and relevant concepts of tensegrity structures are clarified in this section for a better understanding of the proposed method. To this end, the following five assumptions about a tensegrity structure are made:

(A1) Bar and cable members of a tensegrity structure are connected by frictionless pin-joints.

(A2) A level of self-stress is required to stiffen the structure and avoid slacking cable members.

(A3) Mass moments of inertia of bar and cable members along their axial directions are neglected.

(A4) Only axial forces are transmitted in members. Bar members can sustain both tension and compression forces, and cable members can only sustain tension forces. Bending of bar and cable members, and buckling of bar members do not occur.

(A5) Materials of bar and cable members are elastic and homogeneous. Cross-sectional areas are constant along lengths of bar and cable members. Thus, mass distributions of bar and cable members are uniform along their axial directions.

For a general truss structure, the matrix equilibrium equation is

$$M\sigma = l \tag{1}$$

where M is the equilibrium matrix consisting of direction cosines, σ is a vector of generalized stresses, and l is a vector of generalized loads. Because cross-sectional areas and elastic properties of members do not have to be specified and during a form-finding process a tensegrity structure is not subject to any external load, it is convenient to replace σ by a vector of member internal forces and set $l = 0$. Thus, the matrix equilibrium

equation can be written as (Pellegrino and Calladine, 1986)

$$MT = 0 \tag{2}$$

where for a 3-*D* tensegrity structure, M is a $3n \times k$ matrix with n being the number of nodes and k being the number of members, which is obtained from nodal coordinates, and T is a $k \times 1$ vector of member internal forces. The number of mechanisms and states of self-stress of a tensegrity structure can be obtained from the matrix M in Eq. (2).

In this work, it is assumed that a nonlinear dynamic model is developed given an initial equilibrium configuration of a tensegrity structure. Such an equilibrium configuration can be obtained by a procedure in tensegrity structure design, named form finding of the initial equilibrium configuration (FF-IEC) (Yuan and Yang, 2019). The goal of FF-IEC is to determine nodal positions and member internal forces that satisfy Eq. (2) for a tensegrity structure with a predetermined topology. Thus, the tensegrity structure is at a stable equilibrium configuration with a certain level of stiffness. Commonly used methods for FF-IEC can be found in works of Barnes (1999), Zhang and Ohsaki (2006), Lee et al. (2016) and Yuan and Yang (2019).

For tensegrity structures with high surface accuracy requirements and multiple states of self-stress, self-stress determination, which is also called member force assignment or force finding, is an essential part in structural design. During a process of self-stress determination, nodal positions of a tensegrity structure remain unchanged. However, determining self-stress of a tensegrity structure to improve its stiffness and stability (also called optimal self-stress determination), while maintaining its desired configuration, is not well addressed by the form-finding methods introduced above. Because most of the methods are stress-first and displacement-later methods (these methods usually start from assigning a set of member internal forces (or force densities in the force density method (Zhang and Ohsaki, 2006)), and the nodal displacements are then determined by using these assigned member internal forces). In these methods, nodes of a tensegrity structure cannot be freely placed at desired locations and multiple states of self-stress are not fully utilized to improve the stiffness and stability of the structure. In fact, a set of member force distribution can be optimally assigned, so that the stiffness and stability of the tensegrity structure are further improved. Commonly used methods for self-stress determination are seen in works of Tran and Lee (2010), Feng (2017) and Yuan and Zhu (2021). The assigned member internal forces must satisfy unilateral properties (cable members can only sustain tension forces as compared with bar members that can sustain both tension and compression forces) and other member stress constraints upon engineering requirements (for example, member stresses must lie within a specific region to avoid damage).

3. Spatial discretization method for one-dimensional continuous bar and cable members

A tensegrity structure is composed of bar and cable members. These two types of members are in general modeled as elastic rods and taut strings, respectively, which are one-dimensional continuous systems, in nonlinear dynamic modeling and vibration analysis. However, a continuous or distributed-parameter system model is difficult to analyze, since its governing equations are one or more partial differential equations (PDEs). This problem even aggravates when modeling a tensegrity structure, which is usually composed of many bar and cable members placed and connected in a three-dimensional space. This is the case because PDEs are inefficient in handling large-scale systems (systems with many equations and variables) due to the involvement of complicated coordinate transforms.

To resolve this issue, a spatial discretization method (Ren and Zhu, 2013; Wu et al., 2017; Zhu and Ren, 2013) is used to convert PDEs of a continuous system model to a set of ODEs, such that the dynamic response of the system can be revealed by an ODE solver. The spatial discretization method discretizes a continuous system with complicated boundary conditions by separating a displacement of the system into internal terms and boundary-induced terms. The internal terms satisfy certain prescribed simple homogeneous boundary conditions, and the boundary-induced terms account for corresponding boundary conditions that are not satisfied by the internal terms by using additional degrees of freedom at boundaries of the system.

For illustration, applications of the spatial discretization method to one-dimensional continuous bar and cable members are given in this section. Trial functions for both internal and boundary-induced terms obtained in the one-dimensional continuous bar and cable members are used in the CSD method proposed in this paper for nonlinear dynamic modeling and vibration analysis of tensegrity structures in the three-dimensional space.

3.1. Spatial discretization method for a general second-order system

The governing equation of a second-order one-dimensional continuous system can be written in a general form as

$$\alpha \frac{\partial^2 u(\xi,t)}{\partial t^2} + \beta \frac{\partial^2 u(\xi,t)}{\partial \xi^2} = 0, \quad \xi \in (0,1), \quad t > 0 \tag{3}$$

where ξ and t are the independent dimensionless spatial variable and temporal variable, respectively; u is the dependent variable that denotes certain physical quantity; 0 and 1 are boundary locations for the dimensionless spatial variable; and α and β are prescribed coefficients. Boundary conditions of Eq. (3) are given in the general form as

$$\left.\frac{\partial^{s_1} u(\xi,t)}{\partial \xi^{s_1}}\right|_{\xi=0} = e_1(t), \quad \left.\frac{\partial^{s_2} u(\xi,t)}{\partial \xi^{s_2}}\right|_{\xi=1} = e_2(t) \tag{4}$$

where s_1 and s_2 are either 0 or 1, and $e_1(t)$ and $e_2(t)$ are unknown boundary motions.

Let $u(\xi,t)$ be represented in the following form:

$$u(\xi,t) = \widetilde{u}(\xi,t) + \theta_1(\xi)e_1(t) + \theta_2(\xi)e_2(t) \tag{5}$$

where $\theta_i(\xi)$ (i = 1, 2) are corresponding interpolation functions, and $\widetilde{u}(\xi,t)$ is the internal term of the function $u(\xi,t)$. The function $\widetilde{u}(\xi,t)$ is defined to satisfy only simple homogeneous boundary conditions of the system:

$$\left.\frac{\partial^{s_1} \widetilde{u}(\xi,t)}{\partial \xi^{s_1}}\right|_{\xi=0} = 0, \quad \left.\frac{\partial^{s_2} \widetilde{u}(\xi,t)}{\partial \xi^{s_2}}\right|_{\xi=1} = 0 \tag{6}$$

By the spatial discretization method, $\widetilde{u}(\xi,t)$ is expressed in an expansion form as

$$\widetilde{u}(\xi,t) = \sum_{j=1}^{\infty} \varphi_j(\xi) q_j(t) \tag{7}$$

where $\varphi_j(\xi)$ (j = 1, 2, …) are trial functions, which are chosen to be eigenfunctions of a simple self-adjoint system with simple homogeneous boundary conditions, and $q_j(t)$ are corresponding generalized coordinates. The functions $\theta_i(\xi)$ must be properly defined to satisfy the rules given in Eq. (8), so as to satisfy the boundary conditions in Eq. (4):

$$\begin{aligned} &\left.\frac{d^{s_1}\theta_1(\xi)}{d\xi^{s_1}}\right|_{\xi=0} = 1, \quad \left.\frac{d^{s_2}\theta_1(\xi)}{d\xi^{s_2}}\right|_{\xi=1} = 0 \\ &\left.\frac{d^{s_1}\theta_2(\xi)}{d\xi^{s_1}}\right|_{\xi=0} = 0, \quad \left.\frac{d^{s_2}\theta_2(\xi)}{d\xi^{s_2}}\right|_{\xi=1} = 1 \end{aligned} \tag{8}$$

Thus, $u(\xi,t)$ can be expressed by the sum of terms $\widetilde{u}(\xi,t)$ and $\widehat{u}(\xi,t)$ in the spatial discretization method:

$$u(\xi,t) = \widetilde{u}(\xi,t) + \widehat{u}(\xi,t) \tag{9}$$

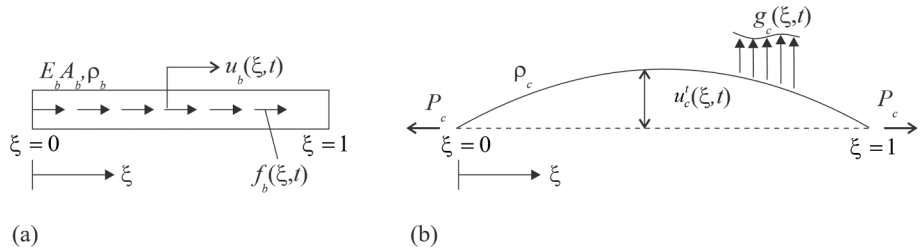

Fig. 1. Displacement and loading of (a) an elastic rod in longitudinal motion and (b) a taut string in transverse motion.

where $\widehat{u}(\xi,t)$ is the boundary-induced term of the function $u(\xi,t)$, defined as

$$\widehat{u}(\xi,t) = \theta_1(\xi)e_1(t) + \theta_2(\xi)e_2(t) \tag{10}$$

According to Eq. (10), the boundary-induced term $\widehat{u}(\xi,t)$ is interpolated from boundary degrees of freedom e_i(t) ($i = 1$ or 2 for a second-order system), which are the dependent variable and/or its spatial derivatives at the boundaries. By substituting Eq. (10) into Eq. (8), $\widehat{u}(\xi,t)$ must satisfy the boundary conditions of the original system:

$$\left.\frac{\partial^{s_1}\widehat{u}(\xi,t)}{\partial\xi^{s_1}}\right|_{\xi=0} = \left.\frac{\partial^{s_1}u(\xi,t)}{\partial\xi^{s_1}}\right|_{\xi=0}, \quad \left.\frac{\partial^{s_2}\widehat{u}(\xi,t)}{\partial\xi^{s_2}}\right|_{\xi=1} = \left.\frac{\partial^{s_2}u(\xi,t)}{\partial\xi^{s_2}}\right|_{\xi=1} \tag{11}$$

By substituting Eqs. (7) and (10) into Eq. (9), the expression of $u(\xi,t)$ has an expansion form

$$u(\xi,t) = \sum_{j=1}^{\infty}\varphi_j(\xi)q_j(t) + \theta_1(\xi)e_1(t) + \theta_2(\xi)e_2(t) \tag{12}$$

It should be noticed that the spatial discretization method can also be applied to a continuous system with a higher order (greater than two), as shown by Wu et al. (2017). Since both bar and cable members of a tensegrity structure are modeled as second-order systems (elastic rods and taut strings), details of applying the spatial discretization method to a higher-order system are not given in this paper.

3.2. Bar and cable models with fixed–fixed boundary conditions

In the proposed CSD method for dynamic modeling of a tensegrity structure, a bar member is modeled as an elastic rod with only a longitudinal displacement (see Fig. 1 (a)). An equation of motion of a one-dimensional bar member in longitudinal vibration can be easily derived by the extended Hamilton's principle as

$$\rho_b\frac{\partial^2 u_b(\xi,t)}{\partial t^2} - E_bA_b\frac{\partial^2 u_b(\xi,t)}{\partial\xi^2} = f_b(\xi,t), \quad \xi\in(0,1), \quad t>0 \tag{13}$$

where ξ is the natural coordinate in the longitudinal direction; t is time; $u_b(\xi, t)$ is the displacement of a differential element $d\xi$; ρ_b is the linear density of the bar member, given in mass per unit length; E_b and A_b are the Young's modulus and cross-sectional area of bar members, assumed constant by assumption (A4); and $f_b(\xi, t)$ is an external load applied in the axial direction of the bar member. In dynamic modeling of a tensegrity structure, fixed–fixed boundary conditions are assumed for structural members. Thus, boundary motions are selected to be the prescribed longitudinal displacements ($e_0(t)$ and $e_1(t)$) at the two ends:

$$e_0(t) = u_b(0,t), \quad e_1(t) = u_b(1,t) \tag{14}$$

By the spatial discretization method, $u_b(\xi,t)$ is expressed as

$$u_b(\xi,t) = \widetilde{u}_b(\xi,t) + \widehat{u}_b(\xi,t) \tag{15}$$

where

$$\widetilde{u}_b(\xi,t) = \sum_{i=1}^{N_b} q_i^b \sin(i\pi\xi), \quad \widehat{u}_b(\xi,t) = (1-\xi)e_0(t) + \xi e_1(t) \tag{16}$$

in which N_b is a positive integer that controls the complexity and accuracy of the method, and q_i^b is the generalized coordinate that describes the internal longitudinal displacement of the bar member. As seen from Eq. (16), the internal term $\widetilde{u}_b$ satisfies the homogeneous boundary conditions. The boundary-induced term $\widehat{u}_b$ satisfies the boundary conditions in Eq. (14) ($\widehat{u}_b(0,t) = e_0(t), \quad \widehat{u}_b(1,t) = e_1(t)$). Note that selection of trial functions for the internal term, and interpolation for the boundary-induced term are not unique. Any selection is considered acceptable if homogeneous boundary conditions and boundary conditions in Eq. (14) are satisfied for the internal term and the boundary-induced term, respectively. It should also be emphasized that the boundary-induced term in Eq. (16) coincides with a shape function in elastic rod modeling in the finite element method (Kan et al., 2018a). So, the finite element method for dynamic modeling of bar members of a tensegrity structure can also be viewed as a simplified version of the CSD method without internal terms.

Cable dynamics has been of great research interest for the past several decades (Sarkar and Manohar, 1996; Starossek, 1991, 1994). A cable member in the proposed CSD method is modeled as a taut string with displacements in both longitudinal and transverse directions. The governing equation of a cable member in the longitudinal direction is the same as that of a bar member given in Eq. (13). So, a dependent variable $u_c^l(\xi,t)$, where $\xi\in(0,1)$, which represents the displacement in the longitudinal direction, can be expressed in the same form as that for a bar member:

$$u_c^l(\xi,t) = \widetilde{u}_c^l(\xi,t) + \widehat{u}_c^l(\xi,t) \tag{17}$$

where

$$\widetilde{u}_c^l(\xi,t) = \sum_{i=1}^{N_l} q_i^l \sin(i\pi\xi), \quad \widehat{u}_c^l(\xi,t) = (1-\xi)e_0(t) + \xi e_1(t) \tag{18}$$

in which N_l is a positive integer that controls the complexity and accuracy of the method, and q_i^l is the generalized coordinate that describes the internal longitudinal displacements of the cable member. Thus, the boundary motions are selected to be the displacements at the two ends in the longitudinal direction:

$$e_0(t) = u_c(0,t), \quad e_1(t) = u_c(1,t) \tag{19}$$

The transverse displacement of a cable member is shown in Fig. 1(b). The equation of motion for a cable member in the transverse vibration can also be easily derived by the extended Hamilton's principle:

$$\rho_c\frac{\partial^2 u_c^t(\xi,t)}{\partial t^2} - \frac{\partial}{\partial\xi}\left(T(\xi)\frac{\partial u_c^t(\xi,t)}{\partial\xi}\right) = g_c(\xi,t), \quad \xi\in(0,1), \quad t>0 \tag{20}$$

where $u_c(\xi, t)$ is transverse displacement of a differential element $d\xi$; ρ_c is the linear density of the cable member, given in mass per unit length; $T(\xi)$ is the tension force in the cable member; and $g_c(\xi, t)$ is an external load applied in the transverse direction of the cable member.

In dynamic modeling of a tensegrity structure, fixed–fixed boundary conditions of structural members are assumed. As will be shown in the next section, in the global Cartesian coordinate system, the transverse displacements at the two ends of a cable member are considered as a combination of its rigid-body motion and longitudinal displacement in

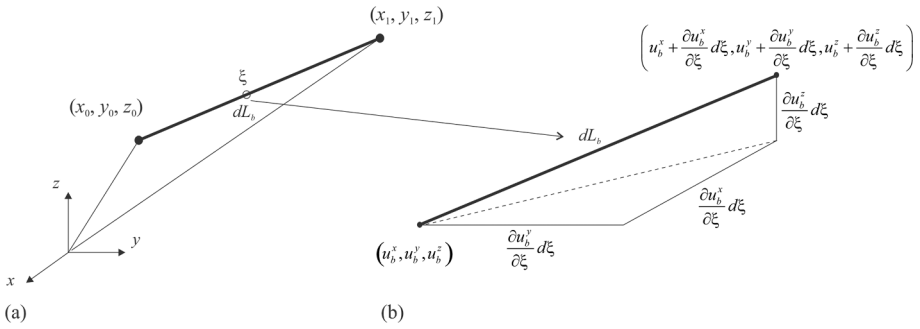

Fig. 2. Motion of a bar member: (a) positions in the global Cartesian coordinate system, and (b) the kinetic diagram of a differential element.

the three-dimensional space. Therefore, boundary motions in the transverse direction are assumed in a homogeneous form

$$u_c^t(0,t) = 0, \quad u_c^t(1,t) = 0 \tag{21}$$

Thus, the boundary-induced term vanishes, which yields an expression of $u_c^t(\xi,t)$ with only the internal terms:

$$u_c^t(\xi,t) = \widetilde{u}_c^t(\xi,t) = \sum_{j=1}^{N_t} q_j^t \sin(j\pi\xi) \tag{22}$$

where N_t is a positive integer that controls the complexity and accuracy of the method, and q_j^t is the generalized coordinate that describes the internal transverse displacement of the member. As seen from Eq. (22), the internal term satisfies the homogeneous boundary condition in Eq. (21).

4. New Cartesian spatial discretization method for three-dimensional bar and cable members of a tensegrity structure

The CSD method for nonlinear dynamic modeling and vibration analysis of tensegrity structures is proposed. The development of dynamic models of three-dimensional bar and cable members of a tensegrity structure is given in this section.

4.1. Nonlinear dynamic model of a bar member

Consider a bar member that connects two nodes of a tensegrity structure in a three-dimensional global Cartesian coordinate system (see Fig. 2(a)). Global Cartesian coordinates of the two nodes are given as (x_0, y_0, z_0) and (x_1, y_1, z_1), respectively. The longitudinal direction of the bar member can be expressed by the position vector $\overrightarrow{R}_b$:

$$\overrightarrow{R}_b = \begin{bmatrix} x_1 - x_0 \\ y_1 - y_0 \\ z_1 - z_0 \end{bmatrix} \tag{23}$$

An independent natural spatial variable $\xi \in [0,1]$ is used to describe an internal position of the bar member. Note that u_b was defined by the spatial discretization method in Section 3 as a displacement, not a position, of a bar member, due to the assumption that the bar member is at an equilibrium state with a zero displacement. However, according to the form finding process introduced in Section 2, an initial equilibrium configuration of a tensegrity structure is determined by assignment of a set of nodal coordinates. Thus, it is convenient to define u_b in Eq. (15) as a position of the bar member for nonlinear dynamic modeling of a tensegrity structure in the three-dimensional space. The internal terms and boundary-induced terms given in Eq. (16) are represented as vector forms in the three-dimensional global Cartesian coordinate system:

$$\widetilde{u}_b(\xi,t) = \sum_{i=1}^{N_b} q_i^b \sin(i\pi\xi)\overrightarrow{r}_b, \quad \widehat{u}_b(\xi,t) = (1-\xi)\begin{bmatrix} x_0 \\ y_0 \\ z_0 \end{bmatrix} + \xi \begin{bmatrix} x_1 \\ y_1 \\ z_1 \end{bmatrix} \tag{24}$$

where q_i^b is the generalized coordinate that describe internal displacements of the bar member in the longitudinal direction; $q_i^b = 0$ means that there is no internal displacement in the longitudinal direction. If the two boundary nodes are fixed, the bar member is at equilibrium when the generalized coordinate q_i^b is zero. The unit vector $\overrightarrow{r}_b = \overrightarrow{R}_b / L_b$ represents the longitudinal direction of the bar member, where L_b is the deformed length of the bar member subject to a level of self-stress (see assumption (A2)):

$$L_b = \sqrt{(x_1 - x_0)^2 + (y_1 - y_0)^2 + (z_1 - z_0)^2} \tag{25}$$

Substituting Eq. (24) into Eq. (15) yields an expression of $u_b(\xi,t)$ in the global Cartesian coordinate system:

$$u_b(\xi,t) = \widetilde{u}_b(\xi,t) + \widehat{u}_b(\xi,t) = \sum_{i=1}^{N_b} \left[q_i^b \sin(i\pi\xi)\overrightarrow{r}_b \right] + (1-\xi)\begin{bmatrix} x_0 \\ y_0 \\ z_0 \end{bmatrix} + \xi \begin{bmatrix} x_1 \\ y_1 \\ z_1 \end{bmatrix} \tag{26}$$

4.1.1. Kinetic energy of a bar member

The velocity $\dot{u}_b(\xi,t)$ of a differential element at the location ξ on the bar member can be obtained by taking the time derivative of Eq. (26):

$$\dot{u}_b(\xi,t) = \dot{\widetilde{u}}_b(\xi,t) + \dot{\widehat{u}}_b(\xi,t) \tag{27}$$

The time derivatives of the internal term $\dot{\widetilde{u}}_b(\xi,t)$ and boundary-induced term $\dot{\widehat{u}}_b(\xi,t)$ are given as

$$\dot{\widetilde{u}}_b(\xi,t) = \sum_{i=1}^{N_b} \left[\dot{q}_i^b \sin(i\pi\xi)\overrightarrow{r}_b + \left(\frac{q_i^b}{L_b}\right)\sin(i\pi\xi)\dot{\overrightarrow{R}}_b - \left(\frac{q_i^b}{L_b}\right)\sin(i\pi\xi)\frac{\dot{L}_b}{L_b}\overrightarrow{R}_b \right] \tag{28}$$

$$\dot{\widehat{u}}_b(\xi,t) = (1-\xi)\begin{bmatrix} \dot{x}_0 \\ \dot{y}_0 \\ \dot{z}_0 \end{bmatrix} + \xi \begin{bmatrix} \dot{x}_1 \\ \dot{y}_1 \\ \dot{z}_1 \end{bmatrix} \tag{29}$$

respectively. Since the internal displacement described by the generalized coordinate q_i^b is usually significantly small than the deformed length of the bar member ($q_i^b \ll L_b$), it can be assumed that

$$\frac{q_i^b}{L_b} \approx 0 \tag{30}$$

By substituting Eq. (30) into Eq. (27), the second and third terms in Eq. (28) vanish. The internal term $\dot{\widetilde{u}}_b(\xi,t)$ of the velocity becomes

$$\dot{\widetilde{u}}_b(\xi,t) = \sum_{i=1}^{N_b} \dot{q}_i^b \sin(i\pi\xi)\overrightarrow{r}_b \tag{31}$$

Substituting Eqs. (31) and (29) into Eq. (27) yields

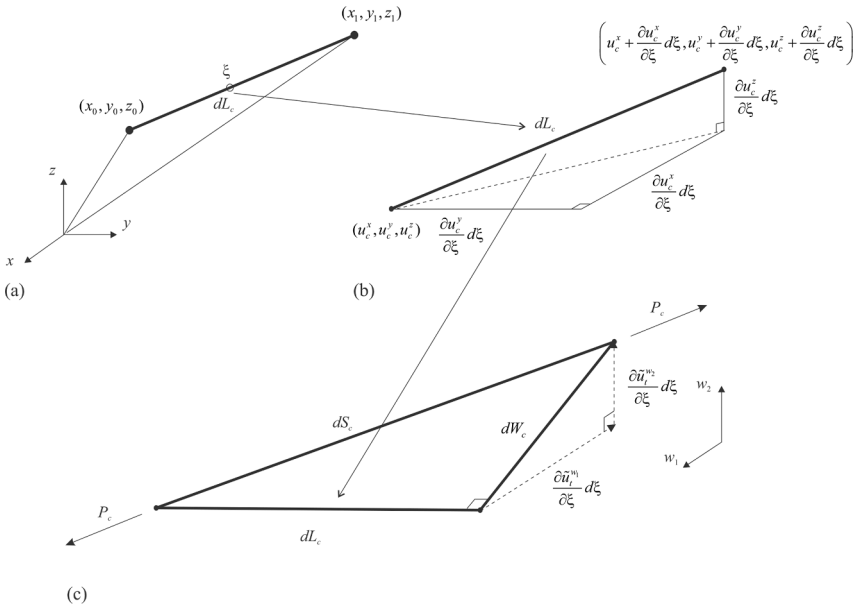

Fig. 3. Motion of a cable member: (a) positions in the global Cartesian coordinate system; (b) the kinetic diagram of a differential element in the longitudinal direction; and (c) the kinetic diagram of a differential element in the transverses directions.

$$\dot{u}_b(\xi,t)=\sum_{i=1}^{N_b}\dot{q}_i^b\sin(i\pi\xi)\vec{r}_b+(1-\xi)\begin{bmatrix}\dot{x}_0\\ \dot{y}_0\\ \dot{z}_0\end{bmatrix}+\xi\begin{bmatrix}\dot{x}_1\\ \dot{y}_1\\ \dot{z}_1\end{bmatrix} \tag{32}$$

Since assumption (A5) states that there is a uniformly distributed mass along the axial direction of the bar member, the mass of the differential element $d\xi$ is $m_b d\xi$, where m_b is the mass of the whole bar member. The kinetic energy of the differential element $d\xi$ on the bar member is given as

$$dT_b=\frac{1}{2}m_b\left\|\dot{u}_b\right\|^2 d\xi \tag{33}$$

Thus, the kinetic energy of the whole bar member can be obtained by integrating Eq. (33) with respect to ξ in the domain [0,1]:

$$T_b=\int_{\xi=0}^{\xi=1}dT_b \tag{34}$$

The explicit form of the kinetic energy of the bar member can be obtained by substituting Eqs. (32) and (33) into Eq. (34):

$$T_b=\frac{1}{2}m_b(T_x+T_y+T_z) \tag{35}$$

where

$$\begin{aligned}
T_x&=\dot{x}_0\dot{x}_1+\frac{1}{3}(\dot{x}_0-\dot{x}_1)^2+\sum_{i=1}^{N_b}\left\{\frac{1}{2}\left(\frac{x_1-x_0}{L_b}\right)^2(\dot{q}_i^b)^2+\frac{2\dot{q}_i^b(x_0-x_1)[i\pi\dot{x}_1\cos(i\pi)-i\pi\dot{x}_0]}{i^2\pi^2L_b}\right\}\\
T_y&=\dot{y}_0\dot{y}_1+\frac{1}{3}(\dot{y}_0-\dot{y}_1)^2+\sum_{i=1}^{N_b}\left\{\frac{1}{2}\left(\frac{y_1-y_0}{L_b}\right)^2(\dot{q}_i^b)^2+\frac{2\dot{q}_i^b(y_0-y_1)[i\pi\dot{y}_1\cos(i\pi)-i\pi\dot{y}_0]}{i^2\pi^2L_b}\right\}\\
T_z&=\dot{z}_0\dot{z}_1+\frac{1}{3}(\dot{z}_0-\dot{z}_1)^2+\sum_{i=1}^{N_b}\left\{\frac{1}{2}\left(\frac{z_1-z_0}{L_b}\right)^2(\dot{q}_i^b)^2+\frac{2\dot{q}_i^b(z_0-z_1)[i\pi\dot{z}_1\cos(i\pi)-i\pi\dot{z}_0]}{i^2\pi^2L_b}\right\}
\end{aligned} \tag{36}$$

4.1.2. Potential energy of a bar member

A differential element of a bar member that starts at the location ξ and ends at the location $\xi+d\xi$ is shown in Fig. 2(b). The global Cartesian coordinates of the starting and ending points of the differential element are given as (u_b^x,u_b^y,u_b^z) and $(u_b^x+\frac{\partial u_b^x}{\partial\xi}d\xi,u_b^y+\frac{\partial u_b^y}{\partial\xi}d\xi,u_b^z+\frac{\partial u_b^z}{\partial\xi}d\xi)$, respectively, where u_b^x, u_b^y and u_b^z are the x-, y- and z-coordinates of $u_b(\xi,t)$ obtained from Eq. (26):

$$\begin{bmatrix}u_b^x\\ u_b^y\\ u_b^z\end{bmatrix}=\sum_{i=1}^{N_b}\left[q_i^b\sin(i\pi\xi)\vec{r}_b\right]+(1-\xi)\begin{bmatrix}x_0\\ y_0\\ z_0\end{bmatrix}+\xi\begin{bmatrix}x_1\\ y_1\\ z_1\end{bmatrix} \tag{37}$$

One can obtain $\frac{\partial u_b^x}{\partial\xi}$, $\frac{\partial u_b^y}{\partial\xi}$ and $\frac{\partial u_b^z}{\partial\xi}$ as

$$\begin{aligned}
\frac{\partial u_b^x}{\partial\xi}&=(x_1-x_0)\left[1+\frac{1}{L_b}\sum\nolimits_{i=1}^{N_b}q_i^b i\pi\cos(i\pi\xi)\right]\\
\frac{\partial u_b^y}{\partial\xi}&=(y_1-y_0)\left[1+\frac{1}{L_b}\sum\nolimits_{i=1}^{N_b}q_i^b i\pi\cos(i\pi\xi)\right]\\
\frac{\partial u_b^z}{\partial\xi}&=(z_1-z_0)\left[1+\frac{1}{L_b}\sum\nolimits_{i=1}^{N_b}q_i^b i\pi\cos(i\pi\xi)\right]
\end{aligned} \tag{38}$$

The deformed length dL_b of the differential element of the bar member can be calculated by the corresponding geometry information shown in Fig. 2(b):

$$dL_b = \sqrt{\left(\frac{\partial u_b^x}{\partial \xi}\right)^2 + \left(\frac{\partial u_b^y}{\partial \xi}\right)^2 + \left(\frac{\partial u_b^z}{\partial \xi}\right)^2}\, d\xi \tag{39}$$

Substituting Eqs. (38) and (25) into Eq. (39) yields an explicit expression of dL_b:

$$dL_b = \left[L_b + \sum_{i=1}^{N_b} q_i^b i\pi \cos(i\pi\xi)\right] d\xi \tag{40}$$

Let the undeformed length of the bar member be L_b^0, and the undeformed length of the differential element be

$$dL_b^0 = L_b^0 d\xi \tag{41}$$

Then, the strain ε_b of the differential element of the bar member at the location ξ is calculated as

$$\varepsilon_b = \frac{dL_b - dL_b^0}{dL_b^0} \tag{42}$$

Based on the linear elasticity assumption, the average internal axial force applied to the differential element from the undeformed length dL_b^0 to the deformed length dL_b is $P_b/2$, where $P_b = E_b A_b \varepsilon_b$ is the tension force.

The work dw_c^b done by the conservative internal force on the differential element is given as

$$dw_c^b = \frac{P_b}{2}(dL_b - dL_b^0) \tag{43}$$

The potential energy V_b of the bar member is then obtained by integrating dw_c^b with respect to ξ in the domain [0,1]:

$$V_b = \int_{\xi=0}^{\xi=1} dw_c^b \tag{44}$$

The explicit form of V_b can be obtained by substituting Eqs. (40)-(43) into Eq. (44):

$$V_b = \frac{E_b A_b (L_b - L_b^0)^2}{2L_b^0} + \frac{E_b A_b \pi^2}{4L_b^0} \sum_{i=1}^{N_b} i^2 (q_i^b)^2 \tag{45}$$

Finally, let the Lagrangian be $L_b^L = T_b - V_b$; the nonlinear equations of motion of a bar member of a tensegrity structure can be obtained by Lagrange's equations

$$\frac{d}{dt}\left(\frac{\partial L_b^L}{\partial \dot{q}_b}\right) - \frac{\partial L_b^L}{\partial q_b} = f_{nc} \tag{46}$$

where q_b are generalized coordinates defined as

$$q_b = \begin{bmatrix} x_0 & y_0 & z_0 & x_1 & y_1 & z_1 & q_1^b & \cdots & q_{N_b}^b \end{bmatrix} \tag{47}$$

and f_{nc} is the generalized force vector associated with nonconservative loads obtained by the virtual work expression.

4.2. Nonlinear dynamic model of a cable member

Consider a cable member that connects two nodes of a tensegrity structure in a three-dimensional global Cartesian coordinate system (see Fig. 3(a)). Global Cartesian coordinates of the two nodes are (x_0, y_0, z_0) and (x_1, y_1, z_1), respectively. The longitudinal direction of the cable member can be expressed by the position vector $\vec{R}_c$:

$$\vec{R}_c = \begin{bmatrix} x_1 - x_0 \\ y_1 - y_0 \\ z_1 - z_0 \end{bmatrix} \tag{48}$$

An independent natural spatial variable $\xi \in [0,1]$ is used to describe an internal position of the cable member. Similar to modeling of bar members in Section 4.1, it is convenient to define u_c as a position, not a displacement, of the cable member for nonlinear dynamic modeling of a tensegrity structure in the three-dimensional space. According to Eqs. (17) and (22), the global coordinate u_c of a differential element of the cable member can be expressed as a summation of internal terms and the boundary-induced term:

$$u_c(\xi, t) = \tilde{u}_c^l(\xi, t) + \tilde{u}_c^t(\xi, t) + \hat{u}_c(\xi, t) \tag{49}$$

Since the cable member is modeled as a taut string with both longitudinal and transverse displacements, the internal term is composed of a corresponding longitudinal term $\tilde{u}_c^l$ and a corresponding transverse term $\tilde{u}_c^t$:

$$\tilde{u}_c^l(\xi, t) = \sum_{i=1}^{N_l} q_i^l \sin(i\pi\xi)\vec{r}_c, \quad \tilde{u}_c^t(\xi, t) = \tilde{u}_{w_1}^t \vec{w}_1 + \tilde{u}_{w_2}^t \vec{w}_2 \tag{50}$$

where

$$\begin{aligned} \tilde{u}_{w_1}^t &= \sum_{j=1}^{N_t} q_j^{t_1} \sin(j\pi\xi) \\ \tilde{u}_{w_2}^t &= \sum_{j=1}^{N_t} q_j^{t_2} \sin(j\pi\xi) \end{aligned} \tag{51}$$

The generalized coordinates q_j^l, $q_j^{t_1}$ and $q_j^{t_2}$ are used to describe internal displacements of the cable member in the longitudinal and transverse directions, respectively; $q_j^l = 0$ means that there is no internal displacement in the longitudinal direction, $(q_j^{t_1}, q_j^{t_2}) = 0$ means that there are no internal displacements in the two transverse directions. Note that the transverse displacements at the two boundary nodes are zero at all time, since the nodal displacement is considered as a combination of the member rigid-body motion and longitudinal displacement in the three-dimensional space by the CSD method. If the two boundary nodes are fixed, the cable member is at equilibrium when the generalized coordinates q_j^l, $q_j^{t_1}$ and $q_j^{t_2}$ are zero. The unit vectors $\vec{r}_c$, $\vec{w}_1$ and $\vec{w}_2$ in Eqs. (50) and (51) are used to represent the longitudinal direction and two transverse directions of the cable member, respectively:

$$\vec{r}_c = \frac{\vec{R}_c}{L_c}, \quad \vec{w}_1 = \frac{\vec{W}_1}{L_1}, \quad \vec{w}_2 = \frac{\vec{W}_2}{L_2} \tag{52}$$

where the unit vectors $\vec{w}_1$ and $\vec{w}_2$ are perpendicular to the longitudinal direction $\vec{r}_c$ of the cable member, and are perpendicular to each other; L_c is the magnitude of the vector $\vec{R}_c$, representing the length of the cable member subject to the longitudinal displacements:

$$L_c = \sqrt{(x_1 - x_0)^2 + (y_1 - y_0)^2 + (z_1 - z_0)^2} \tag{53}$$

L_1 and L_2 are magnitudes of the vectors $\vec{W}_1$ and $\vec{W}_2$, respectively; $\vec{W}_1$ can be defined as one of the three possible forms:

$$\vec{W}_1 = \begin{bmatrix} y_0 - y_1 \\ x_1 - x_0 \\ 0 \end{bmatrix}, \quad \vec{W}_1 = \begin{bmatrix} z_0 - z_1 \\ 0 \\ x_1 - x_0 \end{bmatrix}, \quad \vec{W}_1 = \begin{bmatrix} 0 \\ z_0 - z_1 \\ y_1 - y_0 \end{bmatrix} \tag{54}$$

and $\vec{W}_2$ is obtained by

$$\vec{W}_2 = \vec{R}_c \times \vec{W}_1 \tag{55}$$

The boundary-induced term in Eq. (16) is represented in the three-dimensional global coordinate system as

$$\hat{u}_c(\xi,t) = (1-\xi)\begin{bmatrix} x_0 \\ y_0 \\ z_0 \end{bmatrix} + \xi \begin{bmatrix} x_1 \\ y_1 \\ z_1 \end{bmatrix} \tag{56}$$

According to Eq. (56), $\xi = 0$ represents the location of the node (x_0, y_0, z_0), and $\xi = 1$ represents the location of the node (x_1, y_1, z_1). Then, an expansion form of the global Cartesian coordinate $u_c(\xi, t)$ of the differential element of the cable member at the position ξ is obtained by substituting Eqs. (50) and (56) into Eq. (49):

$$u_c(\xi,t) = \begin{bmatrix} u_l^x & u_l^y & u_l^z \end{bmatrix}^T + \begin{bmatrix} u_t^x & u_t^y & u_t^z \end{bmatrix}^T \tag{57}$$

where

$$\begin{bmatrix} u_l^x & u_l^y & u_l^z \end{bmatrix}^T = (1-\xi)\begin{bmatrix} x_0 & y_0 & z_0 \end{bmatrix}^T + \xi\begin{bmatrix} x_1 & y_1 & z_1 \end{bmatrix}^T + \sum_{i=1}^{N_l} q_i^l sin(i\pi\xi)\vec{r}_c$$
$$\begin{bmatrix} u_t^x & u_t^y & u_t^z \end{bmatrix}^T = \sum_{j=1}^{N_t}\left[q_j^{t_1} sin(j\pi\xi)\vec{w}_1 + q_j^{t_2} sin(j\pi\xi)\vec{w}_2\right] \tag{58}$$

4.2.1. Kinetic energy of a cable member

The velocity $\dot{u}_c(\xi,t)$ of a differential element at ξ on the cable member can be obtained by taking the time derivative of Eq. (49):

$$\dot{u}_c(\xi,t) = \dot{\tilde{u}}_c^l(\xi,t) + \dot{\tilde{u}}_c^t(\xi,t) + \dot{\hat{u}}_c(\xi,t) \tag{59}$$

The time derivatives of the longitudinal and transverse internal terms $\dot{\tilde{u}}_c^l(\xi,t)$ and $\dot{\tilde{u}}_c^t(\xi,t)$, and the boundary-induced term $\dot{\hat{u}}_b(\xi,t)$ are given by

$$\dot{\tilde{u}}_c^l(\xi,t) = \sum_{i=1}^{N_l}\left[\dot{q}_i^l \sin(i\pi\xi)\vec{r}_c + \left(\frac{q_i^l}{L_c}\right)\sin(i\pi\xi)\dot{\vec{R}}_c - \left(\frac{q_i^l}{L_c}\right)\sin(i\pi\xi)\frac{\dot{L}_c}{L_c}\vec{R}_c\right] \tag{60}$$

$$\dot{\tilde{u}}_c^t(\xi,t) = \sum_{j=1}^{N_t}\left[\dot{q}_j^{t_1} sin(j\pi\xi)\vec{w}_1 + \frac{q_j^{t_1}}{L_1} sin(j\pi\xi)\dot{\vec{W}}_1 - \frac{q_j^{t_1}}{L_1} sin(j\pi\xi)\frac{\dot{L}_1}{L_1}\vec{W}_1 + \dot{q}_j^{t_2} sin(j\pi\xi)\vec{w}_2 + \frac{q_j^{t_2}}{L_2} sin(j\pi\xi)\dot{\vec{W}}_2 - \frac{q_j^{t_2}}{L_2} sin(j\pi\xi)\frac{\dot{L}_2}{L_2}\vec{W}_2\right] \tag{61}$$

$$\dot{\hat{u}}_c(\xi,t) = (1-\xi)\begin{bmatrix} \dot{x}_0 \\ \dot{y}_0 \\ \dot{z}_0 \end{bmatrix} + \xi\begin{bmatrix} \dot{x}_1 \\ \dot{y}_1 \\ \dot{z}_1 \end{bmatrix} \tag{62}$$

respectively. Since the internal displacements described by the generalized coordinates q_j^l, $q_j^{t_1}$ and $q_j^{t_2}$ are usually significantly smaller than the deformed length of the cable member, it can be assumed that

$$\frac{q_j^l}{L_c} \approx 0, \quad \frac{q_j^{t_1}}{L_1} \approx 0, \quad \frac{q_j^{t_2}}{L_2} \approx 0 \tag{63}$$

By substituting Eq. (63) into Eqs. (60) and (61), the terms associated with Eq. (63) vanish. The internal terms $\dot{\tilde{u}}_c^l(\xi,t)$ and $\dot{\tilde{u}}_c^t(\xi,t)$ become

$$\dot{\tilde{u}}_c^l(\xi,t) = \sum_{i=1}^{N_l}\left[\dot{q}_i^l \sin(i\pi\xi)\vec{r}_c\right] \tag{64}$$

$$\dot{\tilde{u}}_c^t(\xi,t) = \sum_{j=1}^{N_t}\left[\dot{q}_j^{t_1}\sin(j\pi\xi)\vec{w}_1 + \dot{q}_j^{t_2}\sin(j\pi\xi)\vec{w}_2\right] \tag{65}$$

Substituting Eq. (62) and Eqs. (64) and (65) into Eq. (59) yields an expansion of the velocity of the differential element of the cable member in the global Cartesian coordinate system:

$$\dot{u}_c(\xi,t) = \sum_{i=1}^{N_l}\left[\dot{q}_i^l\sin(i\pi\xi)\vec{r}_c\right] + \sum_{j=1}^{N_t}\left[\dot{q}_j^{t_1}\sin(j\pi\xi)\vec{w}_1 + \dot{q}_j^{t_2}\sin(j\pi\xi)\vec{w}_2\right] + (1-\xi)\begin{bmatrix} \dot{x}_0 \\ \dot{y}_0 \\ \dot{z}_0 \end{bmatrix} + \xi\begin{bmatrix} \dot{x}_1 \\ \dot{y}_1 \\ \dot{z}_1 \end{bmatrix} \tag{66}$$

Since assumption (A5) states that there is a uniformly distributed mass along the axial direction of the cable member, the mass of the differential element $d\xi$ is $m_c d\xi$, where m_c is the mass of the whole cable member. The kinetic energy of the differential element $d\xi$ on the cable member is given as

$$dT_c = \frac{1}{2}m_c\left\|\dot{u}_c\right\|^2 d\xi \tag{67}$$

Thus, the kinetic energy of the entire cable member can be obtained by integrating Eq. (67) with respect to ξ in the domain [0,1]:

$$T_c = \int_{\xi=0}^{\xi=1} dT_c \tag{68}$$

The explicit form of the kinetic energy of the cable member can be obtained by substituting Eqs. (66) and (67) into Eq. (68):

$$T_c = \frac{1}{2}m_c(T_x + T_y + T_z) \tag{69}$$

where

$$\begin{aligned} T_x &= \dot{x}_0\dot{x}_1 + \frac{1}{3}(\dot{x}_0 - \dot{x}_1)^2 + T_x^l + T_x^t + T_x^{l,t} \\ T_y &= \dot{y}_0\dot{y}_1 + \frac{1}{3}(\dot{y}_0 - \dot{y}_1)^2 + T_y^l + T_y^t + T_y^{l,t} \\ T_z &= \dot{z}_0\dot{z}_1 + \frac{1}{3}(\dot{z}_0 - \dot{z}_1)^2 + T_z^l + T_z^t + T_z^{l,t} \end{aligned} \tag{70}$$

Expressions of the terms T_x^l, T_x^t, $T_x^{l,t}$, T_y^l, T_y^t, $T_y^{l,t}$, T_z^l, T_z^t and $T_z^{l,t}$ are given as

$$T_x^l = \frac{x_1 - x_0}{2L_c}\sum_{i=1}^{N_l}\left[\frac{x_1 - x_0}{L_c}\left(\dot{q}_i^l\right)^2 + 4\frac{\dot{x}_0 - \dot{x}_1 cos(i\pi)}{i\pi}\dot{q}_i^l\right]$$
$$T_x^t = \frac{1}{2}\sum_{j=1}^{N_t}\left[\left(\dot{q}_j^{t_1}w_1^x + \dot{q}_j^{t_2}w_2^x\right)^2 + 4\left(\dot{q}_j^{t_1}w_1^x + \dot{q}_j^{t_2}w_2^x\right)\frac{\dot{x}_0 - \dot{x}_1 cos(j\pi)}{j\pi}\right]$$
$$T_x^{l,t} = \frac{x_1 - x_0}{L_c}\sum_{i=1}^{N_l}\sum_{j=1}^{N_t}T_{i,j}^x \tag{71a}$$
$$\text{with} \quad T_{i,j}^x = \begin{cases} \dot{q}_i^l\left(\dot{q}_j^{t_1}w_1^x + \dot{q}_j^{t_2}w_2^x\right), & \text{if} \quad i = j \\ 0, & \text{if} \quad i \neq j \end{cases}$$

$$T_y^l = \frac{y_1 - y_0}{2L_c}\sum_{i=1}^{N_l}\left[\frac{y_1 - y_0}{L_c}\left(\dot{q}_i^l\right)^2 + 4\frac{\dot{y}_0 - \dot{y}_1\cos(i\pi)}{i\pi}\dot{q}_i^l\right]$$
$$T_y^t = \frac{1}{2}\sum_{j=1}^{N_t}\left[\left(\dot{q}_j^{t_1}w_1^y + \dot{q}_j^{t_2}w_2^y\right)^2 + 4\left(\dot{q}_j^{t_1}w_1^y + \dot{q}_j^{t_2}w_2^y\right)\frac{\dot{y}_0 - \dot{y}_1\cos(j\pi)}{j\pi}\right]$$
$$T_y^{l,t} = \frac{y_1 - y_0}{L_c}\sum_{i=1}^{N_l}\sum_{j=1}^{N_t}T_{i,j}^y \tag{71b}$$
$$\text{with} \quad T_{i,j}^y = \begin{cases} \dot{q}_i^l\left(\dot{q}_j^{t_1}w_1^y + \dot{q}_j^{t_2}w_2^y\right), & \text{if} \quad i = j \\ 0, & \text{if} \quad i \neq j \end{cases}$$

$$T_z^l = \frac{z_1 - z_0}{2L_c}\sum_{i=1}^{N_l}\left[\frac{z_1 - z_0}{L_c}\left(\dot{q}_i^l\right)^2 + 4\frac{\dot{z}_0 - \dot{z}_1\cos(i\pi)}{i\pi}\dot{q}_i^l\right]$$

$$T_z^t = \frac{1}{2}\sum_{j=1}^{N_t}\left[\left(\dot{q}_j^{t_1}w_1^z + \dot{q}_j^{t_2}w_2^z\right)^2 + 4\left(\dot{q}_j^{t_1}w_1^z + \dot{q}_j^{t_2}w_2^z\right)\frac{\dot{z}_0 - \dot{z}_1\cos(j\pi)}{j\pi}\right]$$

$$T_z^{l,t} = \frac{z_1 - z_0}{L_c}\sum_{i=1}^{N_l}\sum_{j=1}^{N_t}T_{i,j}^z \tag{71c}$$

$$\text{with}\quad T_{i,j}^z = \begin{cases}\dot{q}_i^l\left(\dot{q}_j^{t_1}w_1^z + \dot{q}_j^{t_2}w_2^z\right), & \text{if}\quad i = j\\ 0, & \text{if}\quad i \neq j\end{cases}$$

where w_1^x, w_1^y, w_1^z, w_2^x, w_2^y and w_2^z are the x-, y- and z-components of the vectors $\vec{w}_1$ and $\vec{w}_2$.

4.2.2. Potential energy of a cable member

The differential element of a cable member that starts at the position ξ and ends at the position $\xi + d\xi$ is shown in Fig. 3(b) and 3(c). The displacement of the differential element is composed of longitudinal and transverse ones. The derivation of the potential energy of a cable member associated with the longitudinal displacement is the same as that of a bar member. By following the procedure in Section 4.1.2, the longitudinal potential energy V_c^l of a cable member is given as

$$V_c^l = \frac{E_cA_c\left(L_c - L_c^0\right)^2}{2L_c^0} + \frac{E_cA_c\pi^2}{4L_c^0}\sum_{i=1}^{N_l}i^2\left(q_i^l\right)^2 \tag{72}$$

After the differential element elongates to the length dL_c due to a longitudinal displacement (see Fig. 3(b)), a transverse displacement is imposed to the same element (see Fig. 3(c)). Under the transverse displacement, the differential element elongates to the length dS. According to geometry information in Fig. 3(c), dS_c, dL_c and dW_c have the following relationship as they form a right triangle:

$$dS_c = \sqrt{\left(dL_c\right)^2 + \left(dW_c\right)^2} \tag{73}$$

where the transverse displacement dW_c is expressed as

$$dW_c = \sqrt{\left(\frac{\partial\tilde{u}_{w_1}^t}{\partial\xi}\right)^2 + \left(\frac{\partial\tilde{u}_{w_2}^t}{\partial\xi}\right)^2}\,d\xi \tag{74}$$

and dL_c is obtained by the procedure given in Eqs. (37)-(40):

$$dL_c = \left[L_c + \sum_{i=1}^{N_l}q_i^l i\pi\cos(i\pi\xi)\right]d\xi \tag{75}$$

Since the transverse displacement of the cable member usually causes little additional change in the member length, it is assumed that the cable tension force P_c can only be changed by longitudinal displacements. In other words, the cable tension remains the same after the transverse displacement is imposed to the differential element of the cable member. Thus, the work done by the tension force on the differential element of the cable member associated with the longitudinal and transverse displacements are independent of each other. The work done by the tension force associated with the transverse displacement is

$$dw_c^t = P_c\left(dS_c - dL_c\right) \tag{76}$$

where $P_c = E_cA_c\varepsilon_c$ is the cable tension force. The strain ε_c of the differential element of the cable member at the location ξ is calculated as

$$\varepsilon_c = \frac{dL_c - dL_c^0}{dL_c^0} \tag{77}$$

The undeformed length dL_c^0 of the differential element is

$$dL_c^0 = L_c^0 d\xi \tag{78}$$

where L_c^0 is the undeformed length of the cable member.

By substituting Eq. (73) into Eq. (76), dw_c^t can be rewritten as

$$dw_c^t = P_c dL_c\left(\sqrt{1 + \left(\frac{dW_c}{dL_c}\right)^2} - 1\right) \tag{79}$$

Since the transverse displacement of the differential element of the cable member is significantly smaller than its deformed length:

$$dW_c \ll dL_c \tag{80}$$

Thus, one has

$$dw_c^t \approx \frac{1}{2}P_c dL_c\left(\frac{dW_c}{dL_c}\right)^2 = \frac{P_c}{2dL_c}\left(dW_c\right)^2 \tag{81}$$

By condition (63) and Eq. (75), one has

$$\frac{1}{dL_c} \approx \frac{1}{L_c}d\xi \tag{82}$$

Substituting Eqs. (74) and (82) into Eq. (81) yields the expanded form of dw_c^t:

$$dw_c^t = \frac{E_cA_c}{2L_cL_c^0}\left[L_c - L_c^0 + \sum_{i=1}^{N_l}q_i^l i\pi\cos(i\pi\xi)\right]\left[\left(\sum_{j=1}^{N_t}q_j^{t_1}j\pi\cos(j\pi\xi)\right)^2 + \left(\sum_{j=1}^{N_t}q_j^{t_2}j\pi\cos(j\pi\xi)\right)^2\right]d\xi \tag{83}$$

The potential energy V_c^t of the cable member associated with the transverse displacement is then obtained by integrating dw_c^t with respect to ξ in the domain [0,1]:

$$V_c^t = \int_{\xi=0}^{\xi=1}dw_c^t \tag{84}$$

The explicit form of V_c^t can be obtained by substituting Eq. (83) into Eq. (84):

$$V_c^t = V_c^{t_1} + V_c^{t_2} \tag{85}$$

where

$$V_c^{t_1} = \frac{E_cA_c\pi^2}{4L_c^0L_c}\left(L_c - L_c^0\right)\sum_{i=1}^{N_t}i^2\left[\left(q_i^{t_1}\right)^2 + \left(q_i^{t_2}\right)^2\right]$$
$$V_c^{t,2} = \sum_{i=1}^{N_l}\sum_{j=1}^{N_t}\sum_{k=1}^{N_t}V_{i,j,k} \tag{86}$$

in which $V_{i,j,k}$ is given as

$$V_{i,j,k} = \begin{cases}\dfrac{E_cA_c}{2L_cL_c^0}\dfrac{j^2q_i^l\pi^3}{i+2j}\left[\left(q_j^{t_1}\right)^2 + \left(q_j^{t_2}\right)^2\right]\left[i^2\cos^2(j\pi) - 2j^2\right], & \text{if}\quad (i=2j)\cap(j=k)\\ \dfrac{v_{i,j,k}}{(i+j+k)(i+j-k)(i-j+k)}, & \text{if}\quad i-j-k=0\\ \dfrac{v_{i,j,k}}{(i+j+k)(i+j-k)(i-j-k)}, & \text{if}\quad i-j+k=0\\ \dfrac{v_{i,j,k}}{(i+j+k)(i-j+k)(i-j-k)}, & \text{if}\quad i+j-k=0\\ 0, & \text{else}\end{cases} \tag{87}$$

with

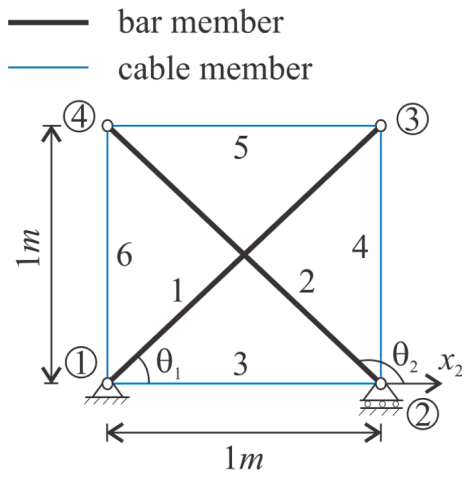

Fig. 4. A planar Snelson's X tensegrity structure.

Table 1
Dimensional and material parameters of cable and bar members of the Snelson's X tensegrity structure.

Parameter	Value
Young's modulus of bar member	183 *GPa*
Young's modulus of cable member	200 *GPa*
Radius of bar member	5 *mm*
Radius of cable member	1 *mm*
Material density of bar member	1750 kg/m^3
Material density of cable member	7850 kg/m^3

$$v_{i,j,k} = -\frac{E_c A_c (-1)^i}{2L_c L_c^0} i^2 jk(j^2 + k^2 - i^2)\pi^3 q_i^l (q_j^{t_1} q_k^{t_1} + q_j^{t_2} q_k^{t_2})\cos(j\pi)\cos(k\pi) \tag{88}$$

The total potential energy of the cable member is obtained by summing terms associated with the longitudinal and transverse displacements:

$$V_c = V_c^l + V_c^t \tag{89}$$

Finally, let the Lagrangian be $L_c^L = T_c - V_c$; the nonlinear equation of motion of a cable member of a tensegrity structure can be obtained by Lagrange's equations

$$\frac{d}{dt}\left(\frac{\partial L_c^L}{\partial \dot{q}_c}\right) - \frac{\partial L_c^L}{\partial q_c} = f_{nc} \tag{90}$$

where q_c are generalized coordinates of the cable member, defined as

$$q_c = \begin{bmatrix} x_0 & y_0 & z_0 & x_1 & y_1 & z_1 & q_1^l & \cdots & q_{N_l}^l & q_1^{t_1} & q_1^{t_2} & \cdots & q_{N_t}^{t_1} & q_{N_t}^{t_2} \end{bmatrix} \tag{91}$$

4.3. Linearized equations of motion for vibration analysis

The nonlinear equations of motion of bar and cable members can be linearized at an equilibrium configuration of a tensegrity structure for its vibration analysis. Denote global nodal coordinates of the two ends of a bar and cable member at the equilibrium state as (x_0^e, y_0^e, z_0^e) and (x_1^e, y_1^e, z_1^e), respectively. Values of other generalized coordinates q^b, q^l, q^{t_1} and q^{t_2} associated with internal longitudinal and transverse displacements are zero at the equilibrium state. Linearized equations of motion of a bar and cable member are given as

$$M_b \ddot{q}_b + K_b q_b = f_{nc} \tag{92}$$

$$M_c \ddot{q}_c + K_c q_c = f_{nc} \tag{93}$$

respectively, where M_b and M_c are the linear mass matrices, and K_b and K_c are the linear stiffness matrices of the bar and cable members, respectively. A dynamic model of the whole tensegrity structure can be assembled in a straight-forward way by using common nodal coordinates of structural members in Eqs. (92) and (93), without a local-to-global coordinate transformation. The linearized dynamic model of the whole tensegrity structure is useful for various analysis and design tasks, such as modal analysis, control system design and structural health monitoring.

The highlight of the proposed CSD method is that internal displacements of structural members are successfully incorporated in the process of nonlinear dynamic modeling of tensegrity structures. The use of generalized coordinates that describe internal displacements of structural members grants the proposed method an ability to achieve accurate dynamic responses of tensegrity structures, especially for vibration analysis in the high-frequency domain. The proposed method is applicable to both simple and complex tensegrity structures, and computationally efficient as it converges in a super-linear rate by using only a small number of internal terms of member displacements. Meanwhile, the use of the global Cartesian coordinate system in the proposed method provides the following advantages: first, a dynamic system of the whole tensegrity structure can be assembled in a fast and straight-forward manner; second, rigid-body motions of structural members are automatically incorporated in the process of dynamic modeling; and third, large-scale and irregular tensegrity structures are effectively handled.

5. Numerical examples

For demonstration of the CSD method, three examples of vibration analysis of tensegrity structures are studied in this section. In the first example, a planar Snelson's X tensegrity structure is investigated for illustrating the use of the CSD method. The second example is a three-dimensional tensegrity tower. The aim of this example is to verify the accuracy and efficiency of the CSD method on a regular tensegrity structure in the three-dimensional space. The third example is an irregular tensegrity structure, which is used to demonstrate the remarkable accuracy and efficiency of the CSD method in handling extremely complicated and irregular tensegrity structures. In the three examples, the CSD method is compared with the Lagrangian method based on generalized coordinates proposed by Sultan and Skelton (2003), the commercial FEA software ANSYS, and the FEA method proposed by Kan et al. (2018a). Approaches to dynamic modeling of tensegrity structures similar to the Lagrangian method based on generalized coordinates can also be found in works of Oppenheim and Williams (2001a), Oppenheim and Williams (2001b) and Kan et al. (2018b), where bar members are treated as rigid bodies and cable members are treated as massless springs; those similar to the FEA methods can also be found in works of Ali and Smith (2010), Faroughi and Lee (2015) and Ma et al. (2022), which assumed uniform material particle distribution along structural members. Note that other dynamic modeling methods, for example, the dynamic stiffness method (Fergusson and Pilkey, 1993), can also potentially predict accurate dynamic responses of tensegrity structures. Therefore, in future research, it is worth investigating the performance of these dynamic modeling methods, while comparing them with the CSD method proposed in this paper.

5.1. A planar Snelson's X tensegrity structure

A planar Snelson's X tensegrity structure with four nodes, two bars and four cables is investigated in the first numerical example. The topology and dimensions of the structure are shown in Fig. 4. Materials of bar and cable members are assumed to be carbon fiber and steel, respectively, with their parameters given in Table 1. The structure is self-stressed, with member internal forces being 141.42 *N* in

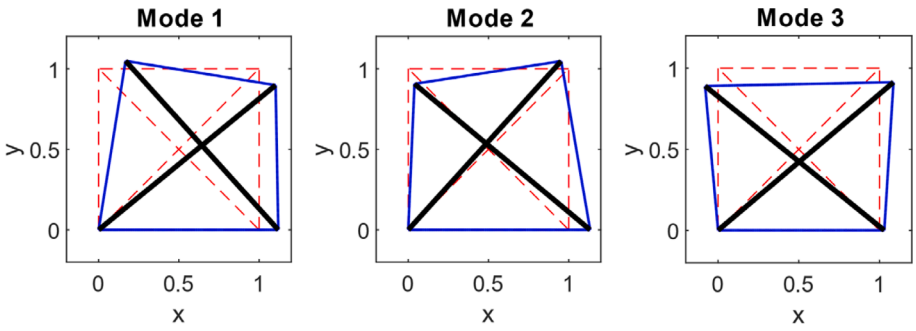

Fig. 5. The three mode shapes of the planar Snelson's X tensegrity structure obtained by the Lagrangian method.

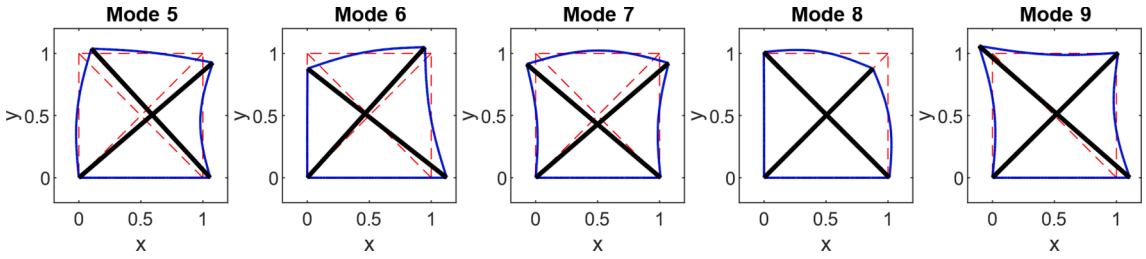

Fig. 6. The fifth throug ninth mode shapes of the planar Snelson's X tensegrity structure obtained by the CSD method.

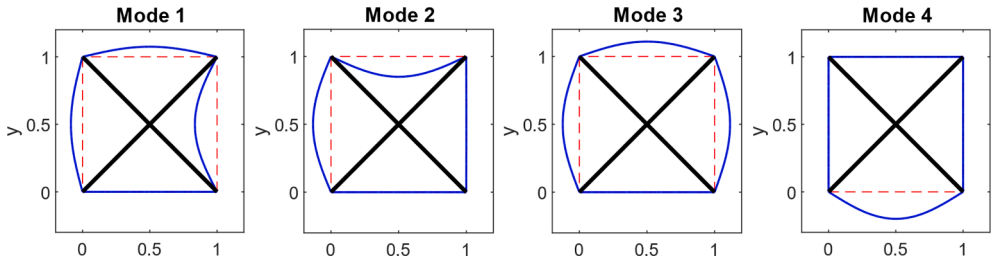

Fig. 7. Mode shapes of the planar Snelson's X tensegrity structure associated with only transverse displacements of cable members.

Table 2
Natural frequencies in Hz of the Snelson's X tensegrity structure obtained by the Lagrangian method and the CSD method for $N_l = 0$ and $N_t = 0$.

	f_1 (f_5)	f_2 (f_6)	f_3 (f_7)	f_4 (f_8)	f_5 (f_9)
Lagrangian method	294.15	495.69	609.96	NA	NA
CSD method $N_b = 0$	259.36	450.22	538.73	1840.94	2675.81
CSD method $N_b = 1$	259.28	448.75	538.72	1722.21	2626.21
CSD method $N_b = 2$	259.28	448.75	538.72	1717.51	2581.14
CSD method $N_b = 3$	259.28	448.73	538.72	1716.63	2580.98

Table 3
Natural frequencies in Hz of the Snelson's X tensegrity structure obtained by the Lagrangian method and the CSD method for $N_b = 0$ and $N_t = 0$.

	f_1 (f_5)	f_2 (f_6)	f_3 (f_7)	f_4 (f_8)	f_5 (f_9)
Lagrangian method	294.15	495.69	609.96	NA	NA
CSD method $N_l = 0$	259.36	450.22	538.73	1840.94	2675.81
CSD method $N_l = 1$	259.25	449.73	538.33	1789.57	2294.10
CSD method $N_l = 2$	259.25	449.70	538.26	1787.75	2291.09
CSD method $N_l = 3$	259.25	449.69	538.25	1787.46	2290.83
CSD method $N_l = 4$	259.25	449.69	538.25	1787.36	2290.66

compression for the two bar members, and 100 N in tension for the four cable members. To eliminate rigid-body motions of the structure, displacements at node one in the x- and the y-directions, and the displacement at node two in the y-direction are restricted to zero.

Table 4
Natural frequencies in Hz of the Snelson's X tensegrity structure obtained by the Lagrangian method and the CSD method for $N_b = 0$ and $N_l = 0$.

	f_1 (f_5)	f_2 (f_6)	f_3 (f_7)	f_4 (f_8)	f_5 (f_9)
Lagrangian method	294.15	495.69	609.96	NA	NA
CSD method $N_t = 0$	259.36	450.22	538.73	1840.94	2675.81
CSD method $N_t = 1$	267.41	455.16	566.35	1891.75	2821.01
CSD method $N_t = 2$	269.05	461.70	568.36	1910.06	2854.01
CSD method $N_t = 3$	270.12	462.23	571.98	1916.04	2873.11
CSD method $N_t = 4$	270.63	464.03	572.52	1920.75	2881.80

5.1.1. Modal analysis

Natural frequencies and mode shapes of the dynamic model of the planar Snelson's X tensegrity structure are calculated by solving the eigenvalue problem of

$$M_{2D}\ddot{Q}_{2D} + K_{2D}Q_{2D} = 0 \tag{94}$$

where M_{2D} and K_{2D} are mass and stiffness matrices of the whole structure, and Q_{2D} is the generalized coordinate vector of the whole structure. These two matrices are obtained through an assembly of mass and stiffness matrices of each member of the structure. For comparison, a dynamic model of the structure is also developed by the Lagrangian method based on the generalized coordinates x_2, θ_1 and θ_2, where x_2 is the horizontal position of node two, and θ_1 and θ_2 are angles of the two bar members with respect to the horizontal direction. The equations of

Table 5
Natural frequencies in Hz associated with cable member transverse displacements of the planar Snelson's X tensegrity structure obtained by the CSD method for $N_b = 0$ and $N_l = 0$.

	f_1	f_5	f_9	f_{13}	f_{17}
$N_t = 1$	31.82	N/A	N/A	N/A	N/A
$N_t = 2$	31.82	63.65	N/A	N/A	N/A
$N_t = 3$	31.82	63.65	95.46	N/A	N/A
$N_t = 4$	31.82	63.65	95.46	127.28	N/A
$N_t = 5$	31.82	63.65	95.46	127.28	159.08

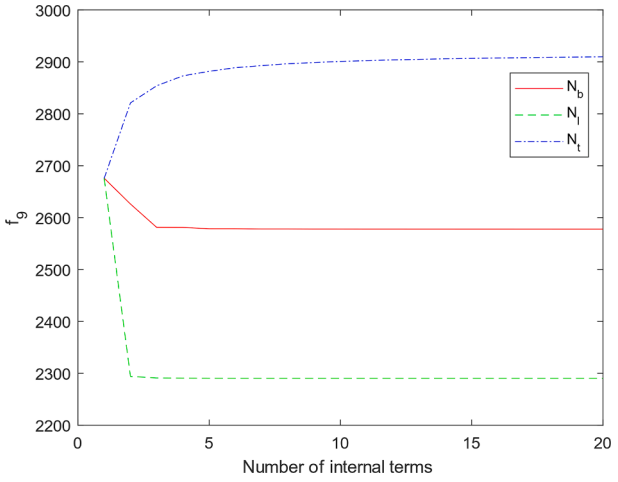

Fig. 8. History of convergence of the natural frequency f_9 of the Snelson's X tensegrity structure.

motion based on the generalized coordinates are derived in Appendix A.

The dynamic model developed by the Lagrangian method has three degrees of freedom, and one can obtain three natural frequencies. All the three natural frequencies are investigated in this example. The three corresponding mode shapes are shown in Fig. 5. For a direct comparison, the fifth through ninth mode shapes associated with nodal modtions obtained by the CSD method for $N_b = 0$, $N_l = 0$ and $N_t = 1$ are presented in Fig. 6. As seen from Figs. 5 and 6, nodal motions of the three mode shapes obtained by the two methods are in good agreement. Different from the Lagrangian method, the CSD method can also reveal the mode shapes associated with bar member elongations (see the fourth and fifth mode shapes in Fig. 6). In addition, the CSD method can also predict transverse motions of cable members within these mode shapes. The first four mode shapes of the dynamic model developed by the CSD method for $N_b = 0$, $N_l = 0$ and $N_t = 1$ are presented in Fig. 7, which shows that the CSD method can also reveal mode shapes associated with transverse displacements of cable members.

The five natural frequencies of the planar Snelson's X tensegrity structure obtained by the two methods are given in Tables 2-4. Note that the three natural frequencies (f_1-f_3) of the dynamic model developed by the Lagrangian method are compared with the natural frequencies of those developed by the CSD method with similar nodal motions of their mode shapes. As observed from the results, accuracy of the natural frequencies can be significantly improved by use of the internal displacement terms in the CSD method. According to Table 2, improvement of 13.45%, 10.46% and 13.22% in accuracies of f_1 (f_5), f_2 (f_6) and f_3 (f_7) are achieved by using three terms of internal displacements of bar members ($N_b = 3$). According to Table 3, improvement of 13.46%, 10.23% and 13.32% in accuracies of f_1 (f_5), f_2 (f_6) and f_3 (f_7) are achieved by using four terms of internal displacements of cable members in longitudinal directions ($N_l = 4$). According to Table 4, improvement of 8.89%, 6.82% and 6.54% in accuracies of f_1 (f_5), f_2 (f_6) and f_3 (f_7) are achieved by using only four terms of internal displacements of cable members in transverse directions ($N_t = 4$).

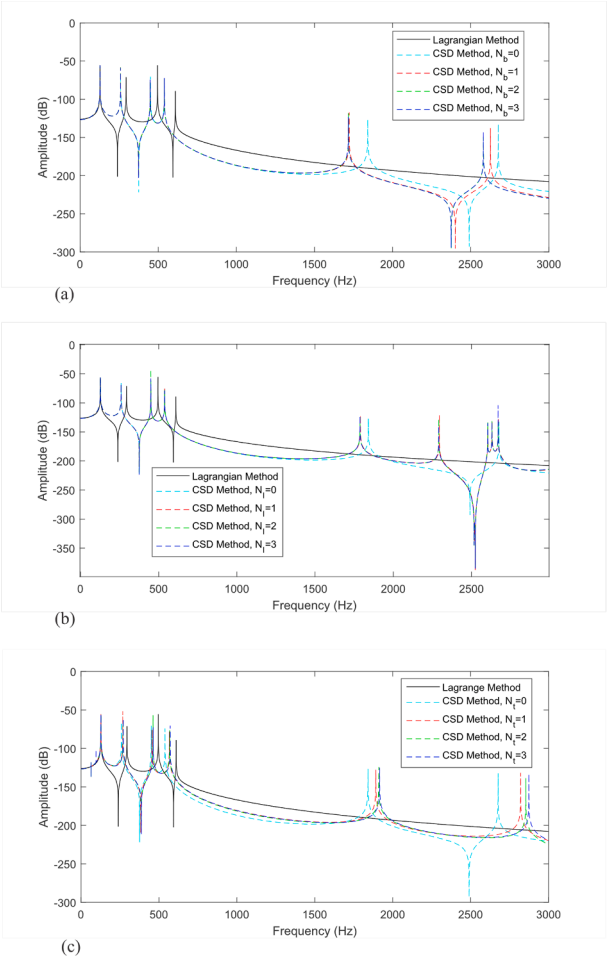

Fig. 9. Frequency responses at node four of the planar Snelson's X tensegrity structure in the y-direction at 0–3000 Hz obtained by the Lagrangian method and the CSD method for: (a) $N_b = 0$–3, $N_l = 0$ and $N_t = 0$; (b) $N_b = 0$, $N_l = 0$–3 and $N_t = 0$; and (c) $N_b = 0$, $N_l = 0$ and $N_t = 0$–3.

The first, fifth, ninth, 13th and 17th natural frequencies, whose mode shapes are associated with only transverse displacements of cable members, of the dynamic model developed by the CSD method are given in Table 5. As seen from the table, the first several natural frequencies associated with transverse displacements of cable members are significantly lower than those associated with nodal motions. This is due to the low stiffness of cable members in their transverse directions.

The history of convergence for the last natural frequency f_9 is shown in Fig. 8. Convergence is defined as follows: the difference of f_9 between two adjacent values of N_b, N_l and N_t is smaller than 0.01%. As observed, the natural frequency f_9 converges in a super-linear rate. Convergence of f_9 is reached at $N_b = 3$, $N_l = 4$ and $N_t = 24$, which shows that the the CSD method can accurately predict natural frequencies of the planar Snelson's X tensegrity structure by using only a small number of internal terms of member displacements.

5.1.2. *Frequency response*

Let a point-wise sinusoidal force $F_f = F_0\sin(2\pi ft)$ be applied at node two of the Snelson's X tensegrity structure in the x-direction with $F_0 = 1000$ N. The frequency response at node four of the structure in the y-direction can be predicted by the Lagrangian method and the CSD method. As seen in Fig. 9, the results of the Lagrangian method and the CSD method do not match. It is shown that consideration of bar members elongations and member internal displacements is essential in predicting accurate dynamic responses of some tensegrity structures in

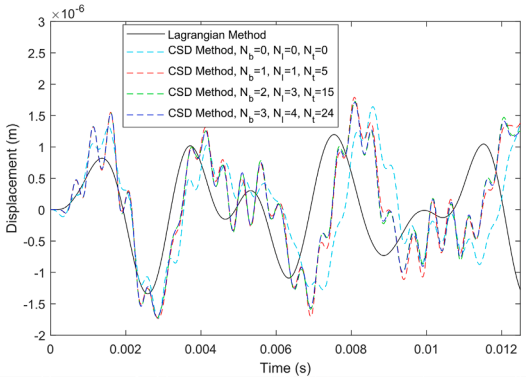

Fig. 10. Displacement at node three of the planar Snelson's X tensegrity structure in the *x*-direction at the excitation frequency of 2000 Hz.

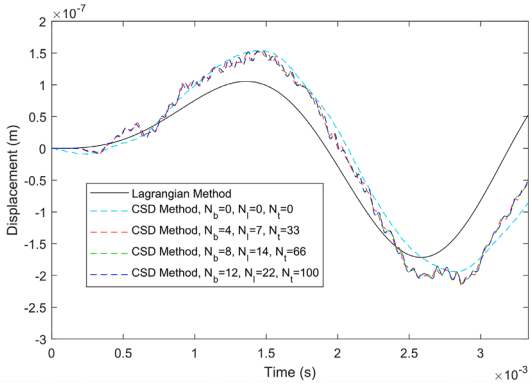

Fig. 11. Displacement at node three of the planar Snelson's X tensegrity structure in the x-direction at the excitation frequency of 15000 Hz.

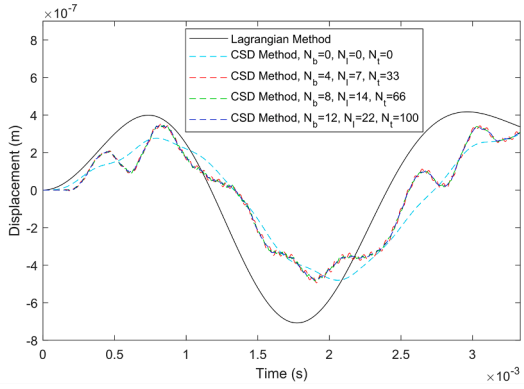

Fig. 12. Displacement at node three of the planar Snelson's X tensegrity structure in the *x*-direction in free vibration.

both low- and high-frequency domains.

As seen in Fig. 9 (a) and (b), the CSD method for $N_b = 0$ and $N_l = 0$, and that for $N_b = 1$–3 and $N_l = 1$–3 are in good agreement under 1000 Hz. This is the case because the natural frequencies revealed by adding internal terms of member longitudinal displacements are above 5000 Hz for $N_b > 0$, and above 2600 Hz for $N_l > 0$. However, Fig. 9 (c) shows that the results of the CSD method for $N_t = 0$ and that for $N_t > 0$ do not match under 500 Hz when internal terms of cable member transverse displacements are used ($N_t > 0$) by the CSD method. This is due to the fact that the natural frequencies associated with cable member transverse displacements are in a lower frequency range (under 50 Hz). Thus, these results show that the CSD method can provide more accurate dynamic

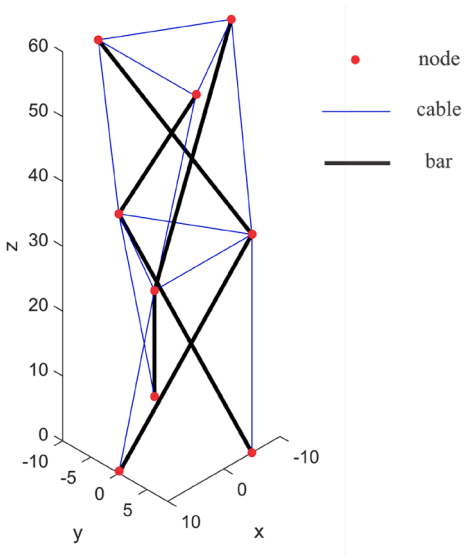

Fig. 13. A three-dimensional tensegrity tower.

responses in a low-frequency domain. It is also shown that in the frequency range of 1500–3000 Hz, which is near the natural frequencies f_4 and f_5 of the dynamic model developed by the CSD method for $N_b = 0$, $N_l = 0$ and $N_t = 0$, the use of any type of internal terms of member displacements ($N_b > 0$, $N_l > 0$ and $N_t > 0$) by the CSD method can significantly improve the accuracy of frequency response prediction.

5.1.3. *Transient response*

Let a point-wise sinusoidal force $F_f = F_0 \sin(2\pi ft)$ be applied at node two of the Snelson's X tensegrity structure in the *x*-direction with $F_0 = 10$ *N*. The transient responses at node three of the structure in the *x*-direction are plotted in Figs. 10 and 11 at excitation frequencies of 2000 Hz and 15000 Hz, respectively. In both cases, the solutions obtained by the Lagrangian method are inaccurate, compared with the CSD method. As observed from Fig. 10, the CSD method can accurately predict the transient response for the 2000 Hz excitation frequency by using only a small number of internal terms of member displacements. The results for $N_b = 1$–3, $N_l = 1$–4 and $N_t = 5$–24 obtained by the CSD method are in good agreement, which shows a trend of convergence. As observed from Fig. 11, only the CSD method can reveal the high-frequency responses for the 15000 Hz excitation frequency. Note that the high-frequency vibration of node two cannot be captured by the Lagrangian method. The results for $N_b = 8$–12, $N_l = 14$–22 and $N_t = 66$–100 obtained by the CSD method are in good agreement, which shows a trend of convergence, while the result for $N_b = 4$, $N_l = 14$ and $N_t = 33$ is inaccurate. This is the case because more internal terms of member displacements are needed by the CSD method to accurately predict dynamic responses of a tensegrity structure in the high-frequency domain.

The transient response of the planar Snelson's X tensegrity structure in free vibration at node three in the *x*-direction is plotted in Fig. 12, with the initial displacement at node two in the *x*-direction being 1×10^{-6} *m*. Initial conditions for all other nodes and member internal displacements are at the initial equilibrium configuration of the structure. Similar to the results for forced vibration, the Lagrangian method cannot accurately predict dynamic responses of the structure in free vibration. For the CSD method, more internal terms of member displacements are needed if dynamic responses in the high-frequency domain need to be accurately revealed.

5.2. *A three-dimensional tensegrity tower*

A three-dimensional tensegrity tower with nine nodes, six bars and 12 cables, which is similar to the structure studied by Ma et al. (2022), is

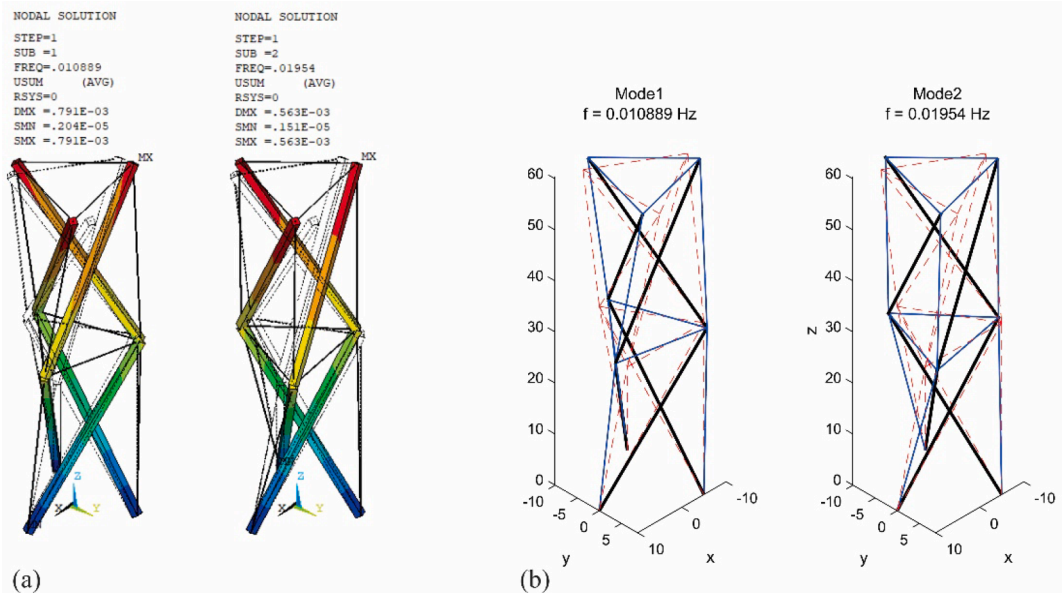

Fig. 14. The first two mode shapes of the dynamic model of the three-dimensional tensegrity tower developed by: (a) ANSYS; and (b) the CSD method for $N_b = 0$, $N_l = 0$ and $N_t = 0$.

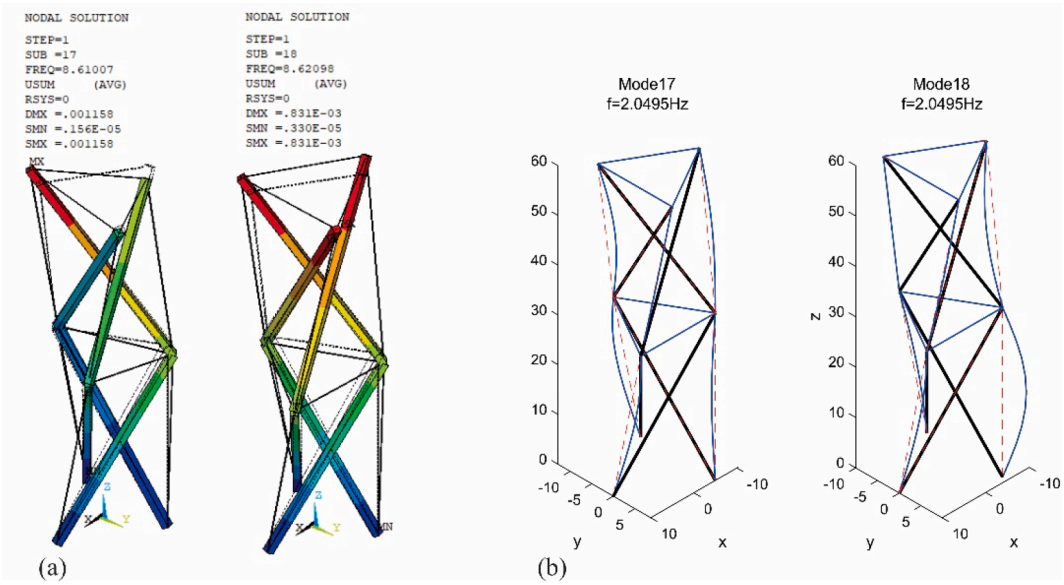

Fig. 15. The 17th and 18th mode shapes of the dynamic model of the three-dimensional tensegrity tower developed by: (a) ANSYS; and (b) the CSD method for $N_b = 0$, $N_l = 0$ and $N_t = 1$.

Table 6
The first, second, 17th and 18th natural frequencies in Hz of the three-dimensional tensegrity tower obtained by ANSYS and the CSD method.

	f_1	f_2	f_{17}	f_{18}
ANSYS	0.0109	0.0195	8.6101	8.6210
CSD Method $N_b = 0$, $N_l = 0$, $N_t = 0$	0.0109	0.0195	8.6100	8.6210
CSD Method $N_b = 3$, $N_l = 3$, $N_t = 3$	0.0109	0.0195	2.0495	2.0495

investigated here as the second numerical example. A perspective view of the structure is shown in Fig. 13, with nodal coordinates given in Appendix B. The material parameters, topology and member internal forces of the structure are given in Appendix B, where compression and tension forces are given as negative and positive values, respectively. Positions of nodes one, two and three in the x-, y- and z-directions are fixed for elimination of rigid-body motions of the tensegrity tower. In this example, the proposed CSD method is compared with the commercial FEA software ANSYS.

5.2.1. Modal analysis

Natural frequencies and mode shapes of the three-dimensional tensegrity tower are calculated by solving the eigenvalue problem of

$$M_{tower}\ddot{Q}_{tower} + K_{tower}Q_{tower} = 0 \tag{95}$$

where M_{tower} and K_{tower} are mass and stiffness matrices of the whole structure, respectively, and Q_{tower} is the generalized coordinate vector of the whole structure. These two matrices are obtained through an assembly of mass and stiffness matrices of each member of the structure.

The dynamic model of the three-dimensional tensegrity tower developed by ANSYS has 18 degrees of freedom, and can thus yield 18

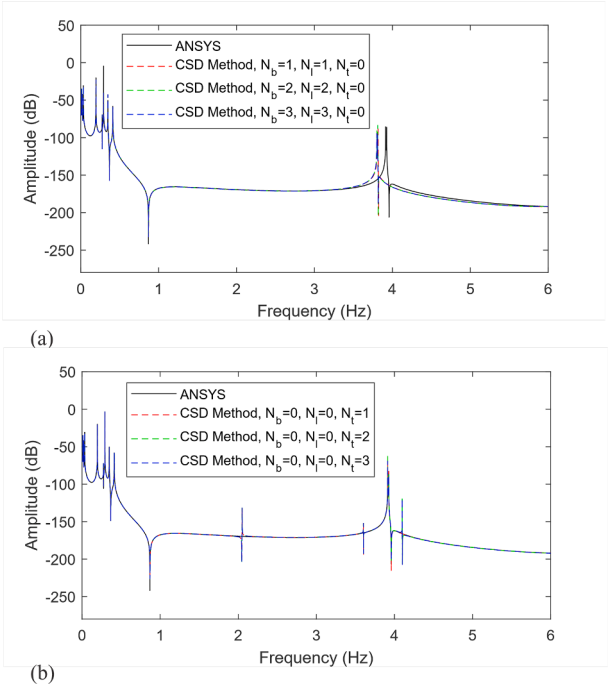

Fig. 16. Frequency responses at node six of the three-dimensional tensegrity tower in the z-direction at 0–6 Hz obtained by ANSYS and the CSD method for: (a) $N_b = 1$–3, $N_l = 1$–3 and $N_t = 0$; and (b) $N_b = 0$, $N_l = 0$ and $N_t = 1$–3.

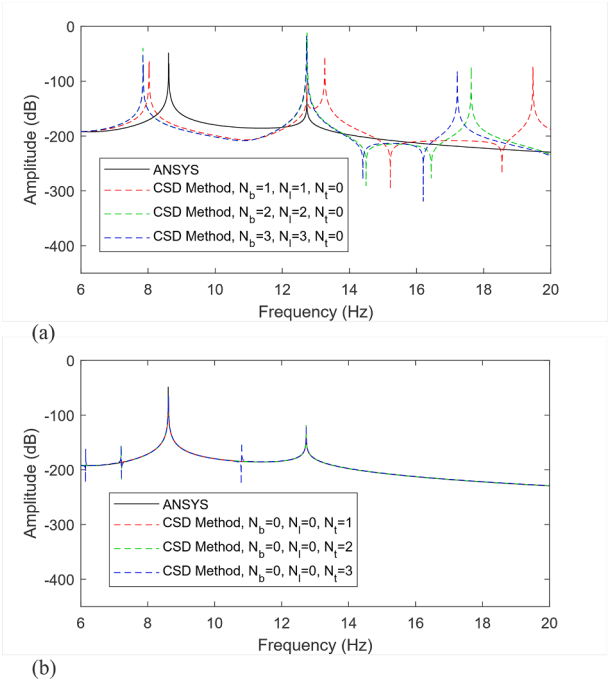

Fig. 17. Frequency responses at node six of the three-dimensional tensegrity tower in the z-direction at 6–20 Hz obtained by ANSYS and the CSD method for: (a) $N_b = 1$–3, $N_l = 1$–3 and $N_t = 0$; and (b) $N_b = 0$, $N_l = 0$ and $N_t = 1$–3.

natural frequencies. The first two mode shapes obtained by ANSYS and the CSD method for $N_b = 0$, $N_l = 0$ and $N_t = 0$ are shown in Fig. 14 for a direct comparison. As observed, the nodal motions of the two mode shapes obtained by the two methods are in good agreement, which shows the correctness of the CSD method. The 17th and 18th mode shapes obtained by ANSYS and the CSD method for $N_b = 0$, $N_l = 0$ and $N_t = 1$ are given in Fig. 15. As observed, the mode shapes obtained by the

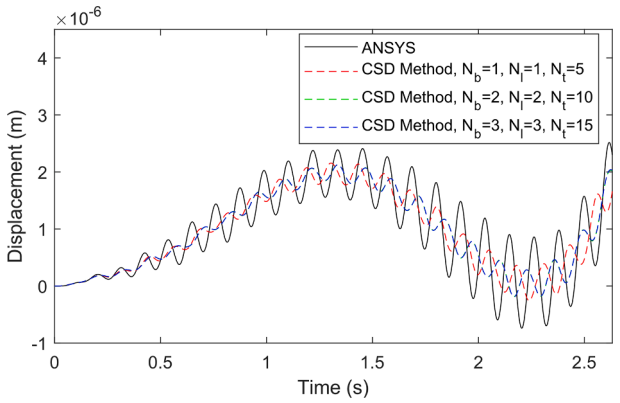

Fig. 18. Displacement at node six of the three-dimensional tensegrity tower in the z-direction at the excitation frequency of 9.5 Hz.

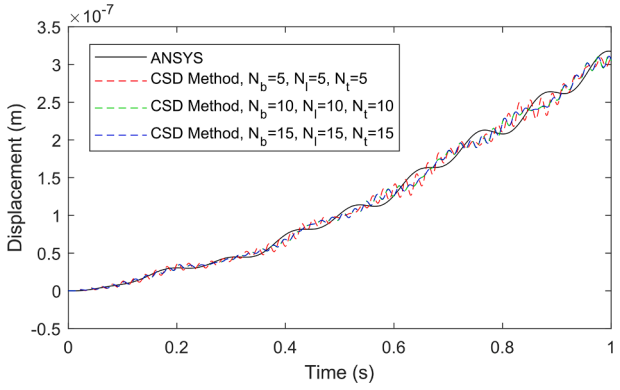

Fig. 19. Displacement at node six of the three-dimensional tensegrity tower in the z-direction at the excitation frequency of 50 Hz.

two methods are different. This is the case because the CSD method can also reveal mode shapes associated with transverse displacements of cable members, while these mode shapes cannot be obtained by ANSYS.

The natural frequencies obtained by ANSYS and the CSD method are compared in Table 6. As seen from the table, the natural frequencies f_1, f_2, f_{17} and f_{18} obtained by ANSYS and the CSD method without using internal terms of member displacements ($N_b = 0$, $N_l = 0$, $N_t = 0$) are in good agreement, which shows the correctness of the CSD method. The use of internal terms of member displacements by the CSD method ($N_b = 3$, $N_l = 3$, $N_t = 3$) provides little impact on the first two natural frequencies. On the other hand, the use of internal terms of member displacements shows a strong impact on the values of f_{17} and f_{18}. This is the case because the natural frequencies f_{17} and f_{18} obtained by the CSD method for $N_b = 3$, $N_l = 3$ and $N_t = 3$ are for modes shapes that cannot be revealed by ANSYS or the CSD method for $N_b = 0$, $N_l = 0$ and $N_t = 0$.

5.2.2. *Frequency response*

Let a point-wise sinusoidal force $F_f = F_0\sin(2\pi ft)$ be applied at node nine of the three-dimensional tensegrity tower in the z-direction with $F_0 = 10000$ N. The frequency response at node six in the z-direction of the structure is predicted by ANSYS and the CSD method in Figs. 16 and 17. As seen in Fig. 16 (a), the two methods are in good agreement under 6 Hz for $N_b = 1$–3 and $N_l = 1$–3. This is the case because the natural frequencies revealed by adding internal terms of member longitudinal displacements are above 13 Hz for $N_b > 0$, and above 50 Hz for $N_l > 0$. However, the results in Fig. 16 (b) show that the results obtained by ANSYS cannot reveal some peaks of the results obtained by the CSD method when internal terms of cable member transverse displacements are used ($N_t > 0$). This is due to the fact that these peaks are the natural

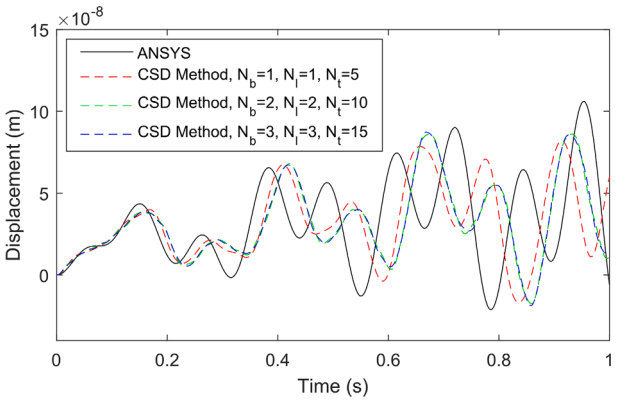

Fig. 20. Displacement at node six of the three-dimensional tower in the z-direction in free vibration.

frequencies associated with transverse displacements of cable members, which can only be revealed by the CSD method. In the frequency range of 6–20 Hz, the results in Fig. 17 show that the use of all three types of internal terms (longitudinal displacement terms of bar and cable members, and transverse displacement terms of cable members) by the CSD method can significantly improve the accuracy of the frequency response of the three-dimensional tensegrity tower, as compared with those obtained from ANSYS.

5.2.3. Transient response

Let a point-wise sinusoidal force $F_f = F_0 \sin(2\pi ft)$ be applied at node nine of the three-dimensional tensegrity tower in the z-direction with $F_0 = 10000$ N. The transverse displacements at node six of the structure in the z-direction are plotted in Figs. 18 and 19 at excitation frequencies of 9.5 Hz and 50 Hz, respectively. As observed from Fig. 18, the results obtained by the CSD method for $N_b = 2$–3, $N_l = 2$–3 and $N_t = 10$–15 are in good agreement, which shows a trend of convergence. However, the results obtained by the CSD method for $N_b = 1$, $N_l = 1$ and $N_t = 5$, and those by ANSYS are inaccurate. As observed from Fig. 19, only the CSD method can accurately predict dynamic responses of the structure at the 50 Hz excitation frequency and reveal the high-frequency vibration, while the high-frequency vibration of node six cannot be captured by ANSYS. The results for $N_b = 10$–15, $N_l = 10$–15 and $N_t = 10$–15 obtained by the CSD method are in good agreement, which shows a trend of convergence, while the results obtained by the CSD method for $N_b = 5$, $N_l = 5$ and $N_t = 5$, and those by ANSYS are inaccurate. This is the case because more internal terms of member displacements are needed by the CSD method to accurately predict dynamic responses of a tensegrity structure in the high-frequency domain.

The transient response of the three-dimensional tensegrity tower in free vibration at node six in the z-direction is plotted in Fig. 20, with the initial displacement at node nine in the z-direction being 1×10^{-5} m. Initial conditions for all other nodes and member internal displacements are at the initial equilibrium configuration of the structure. Similar to the results of forced vibration, as shown in Fig. 20, the results obtained by the CSD method for $N_b = 1$, $N_l = 1$ and $N_t = 5$ and those by ANSYS are inaccurate. The results obtained by the CSD method with $N_b = 2$–3, $N_l = 2$–3 and $N_t = 10$–15 are in good agreement, which shows a trend of convergence.

5.3. An irregular tensegrity grid

In this example, a largely distorted tensegrity grid with an irregular layout is studied to demonstrate the efficiency of the CSD method in handling a large-scale irregular tensegrity structure. The irregular topology layout of this structure was first introduced by Shekastehband et al. (2013). In this work, nodal positions are changed to form a complete irregular tensegrity structure, as shown in Fig. 21. This structure is composed of 40 nodes, 36 bars and 84 cables with six rigid-body mechanisms, three internal mechanisms, and nine states of self-stress. Although this structure has internal mechanisms, it can still be a stable structure by properly assigning member internal forces. Materials of bar and cable members are assumed to be carbon fiber and steel, respectively, with their parameters being the same as those in the first numerical example given in Table 1. An initial equilibrium configuration of the irregular tensegrity structure is determined by the stochastic fixed nodal displacement method proposed by Yuan and Zhu (2021). Positions of nodes one, 23 and 34 in the x-, y- and z-directions are fixed for elimination of rigid-body motions of the structure. The proposed CSD method is compared with the FEA method proposed by Kan et al. (2018a).

Table 7
Comparison of the first five natural frequencies in Hz of the irregular tensegrity grid.

	f_1	f_2	f_3	f_4	f_5
FEA method	71.01	159.72	219.96	233.57	295.50
CSD method	70.98	159.27	218.92	232.60	293.41

Table 8
Comparison of the sixth to the 10th natural frequency in Hz of the irregular tensegrity grid.

	f_6	f_7	f_8	f_9	f_{10}
FEA method	472.31	475.66	621.61	639.25	888.51
CSD method	459.07	460.37	489.10	494.77	500.52

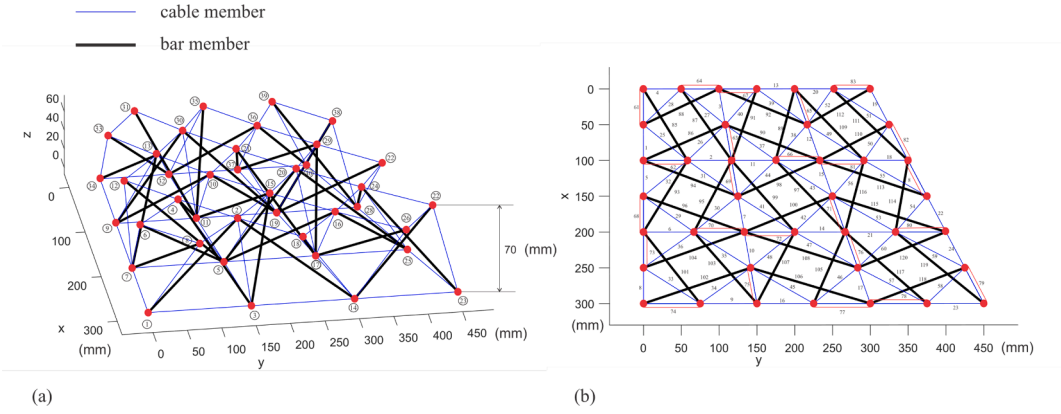

Fig. 21. An irregular tensegrity grid: (a) the perspective view and (b) the top view.

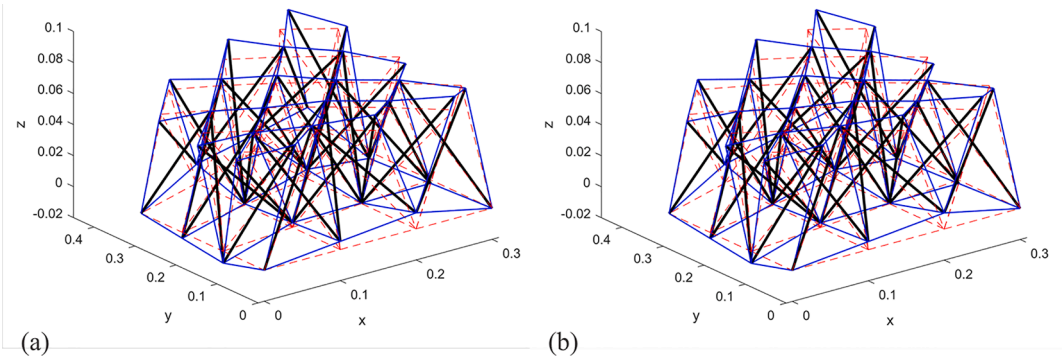

Fig. 22. The first mode shapes of the irregular tensegrity grid obtained by (a) the FEA method and (b) the CSD method.

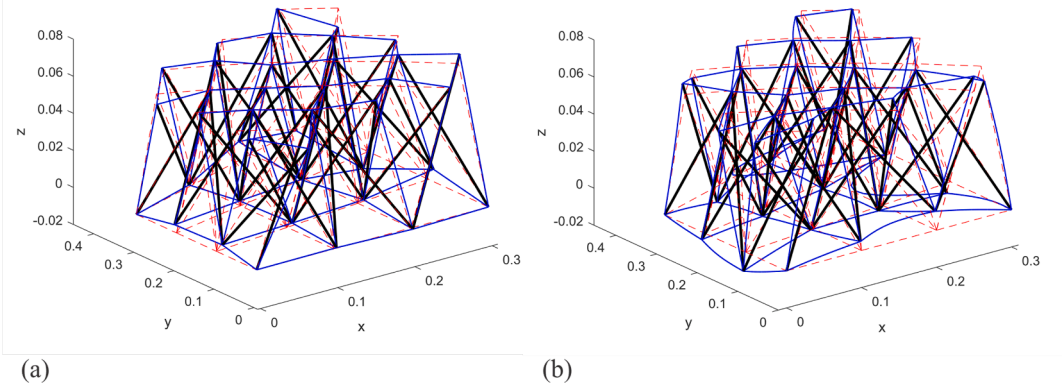

Fig. 23. The 10th mode shapes of the irregular tensegrity grid obtained by (a) the FEA method and (b) the CSD method.

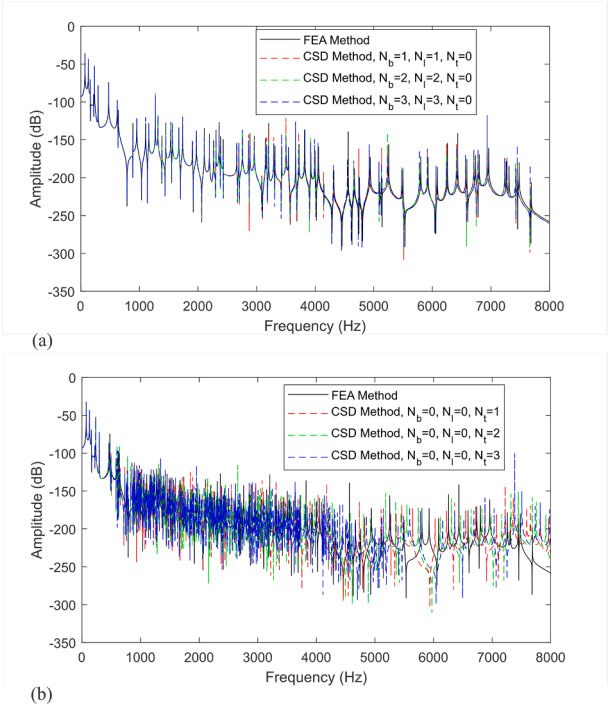

Fig. 24. Frequency responses at node 16 of the irregular tensegrity grid in the z-direction at 0–8000 Hz obtained by the FEA method and the CSD method for: (a) $N_b = 1$–3, $N_l = 1$–3 and $N_t = 0$; and (b) $N_b = 0$, $N_l = 0$ and $N_t = 1$–3.

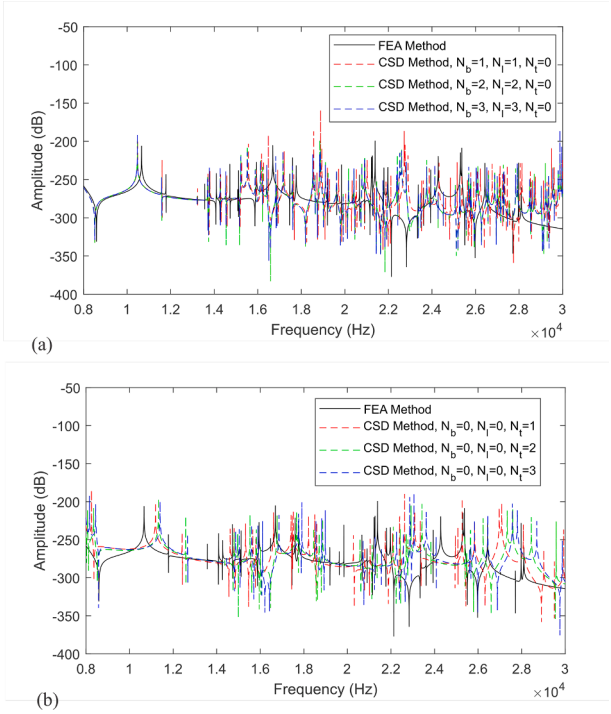

Fig. 25. Frequency responses at node 16 of the irregular tensegrity grid in the z-direction at 8000–30000 Hz obtained by the FEA method and the CSD method for: (a) $N_b = 1$–3, $N_l = 1$–3 and $N_t = 0$; and (b) $N_b = 0$, $N_l = 0$ and $N_t = 1$–3.

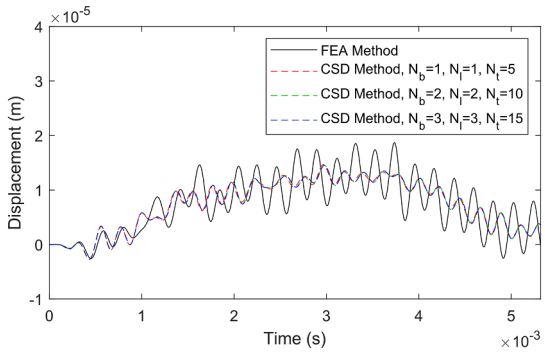

Fig. 26. Displacement at node 16 of the irregular tensegrity grid in the z-direction at the excitation frequency of 4700 Hz.

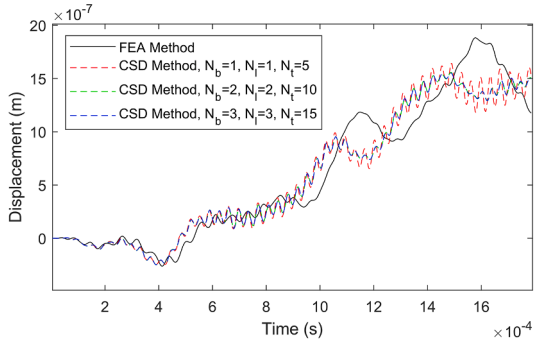

Fig. 27. Displacement at node 16 of the irregular tensegrity grid in the z-direction at the excitation frequency of 28000 Hz.

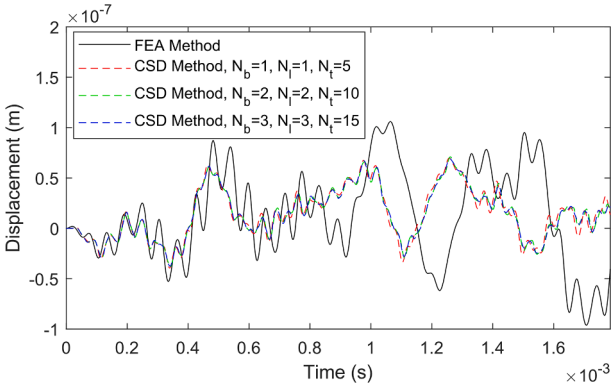

Fig. 28. Displacement at node 16 of the irregular tensegrity grid in the z-direction in free vibration.

5.3.1. Modal analysis

The first 10 natural frequencies (f_1-f_{10}) of dynamic models of the irregular tensegrity grid developed by the FEA method and the CSD method for $N_b = 1$, $N_l = 1$ and $N_t = 1$ are investigated, with the results given in Tables 7 and 8. The corresponding first and 10th mode shapes are shown in Figs. 22 and 23, respectively. As seen in Table 7, the natural frequencies f_1-f_5 obtained by the two methods are in good agreement, with errors being less than 1%. However, the results in Table 8 show that the natural frequencies f_6-f_{10} obtained by the two methods do not match, with errors being 2.88%-77.52%. It can also be observed that the mode shapes obtained by the two methods are similar to each other when the corresponding natural frequencies are close to each other (see Fig. 22 that shows the first mode shape as an example). However, the mode shapes obtained by the two methods are different when there is a significant deviation between the corresponding natural frequencies, see Fig. 23 that shows the 10th mode shape as an example, since the CSD method can yield modes that cannot be revealed by the FEA method even in the low-frequency domain.

5.3.2. Frequency response

Let a point-wise sinusoidal force $F_f = F_0\sin(2\pi ft)$ be applied at node 39 of the irregular tensegrity grid in the z-direction with $F_0 = 1000$ N. The frequency responses at node 16 of the structure in the z-direction are obtained by the FEA method and the CSD method at 0–30000 Hz and plotted in Figs. 24 and 25. As seen in Fig. 24 (a), the FEA method and the CSD method are in good agreement under 8000 Hz for $N_b = 1$–3 and $N_l = 1$–3. This is the case because the natural frequencies obtained by the CSD method associated with internal terms of member longitudinal displacements are above 30000 Hz for $N_b > 0$, and above 15000 Hz for $N_l > 0$, which are far from 8000 Hz. However, Fig. 24 (b) shows that the results of the two methods match only under 500 Hz when internal terms of cable member transverse displacements are used ($N_t > 0$) by the CSD method. This is due to the fact that the natural frequencies associated with cable member transverse displacements are in a lower frequency range (450 Hz and above), which shows that the CSD method can provide a more accurate dynamic response than the FEA method even in a low-frequency domain. In the frequency range of 8000–30000 Hz, the results in Fig. 25 show that the use of all three types of internal terms (longitudinal displacement terms of bar and cable members, and transverse displacement terms of cable members) by the CSD method can significantly improve the accuracy of the frequency response predicted, as compared with the FEA method.

5.3.3. Transient response

Let a point-wise sinusoidal force $F_f = F_0\sin(2\pi ft)$ be applied at node 39 of the irregular tensegrity grid in the z-direction with $F_0 = 100$ N. The displacements at node 16 of the structure in the z-direction are plotted in Figs. 26 and 27, at excitation frequencies of 4700 Hz and 28000 Hz, respectively. As observed from Fig. 26, the results obtained by the CSD method for different values of N_b, N_l and N_t are in good agreement, which shows a fast trend of convergence. However, significant differences between the results obtained by the FEA method and the CSD method are observed. As observed from Fig. 27, only the CSD method can reveal the high-frequency responses for the 28000 Hz excitation frequency. The results for $N_b = 2$ and 3, $N_l = 2$ and 3, and $N_t = 10$ and 15 obtained by the CSD method are in good agreement. However, the dynamic responses obtained by the CSD method for $N_b = 1$, $N_l = 1$ and $N_t = 5$, and those by the FEA method are inaccurate. It is thus shown that the CSD method can accurately predict dynamic responses of the irregular tensegrity grid in the high-frequency domain. The use of more internal terms of member displacements are required by the CSD method to provide convergence for high excitation frequencies.

The transient response at node 16 of the irregular tensegrity grid in the z-direction in free vibration is plotted in Fig. 28, with the initial displacement at node 39 in the z-direction being 1×10^{-6} m. Initial conditions for all other nodes and member internal displacements are at the initial equilibrium configuration of the structure. As shown in Fig. 28, the results obtained by the CSD method for different values of N_b, N_l and N_t are in good agreement, which shows a fast trend of convergence. However, significant differences between the results obtained by the two methods are observed. Therefore, the efficiency and accuracy of the CSD method in predicting dynamic responses of the irregular tensegrity structure in free vibration are verified.

As observed from the simulation results of the three numerical examples, the following conclusion about the CSD method can be made: 1) The CSD method can reveal more modes of a tensegrity structure than the Lagrangian method based on generalized coordinates and the FEA method. These revealed modes can have either local mode shapes associated with only member internal displacements, or global mode shapes in which nodal motions and member internal displacements are

coupled. 2) More internal terms of member displacements are needed for the CSD method if the dynamic response in the high-frequency domain needs to be revealed. 3) It is shown that the dynamic response of a tensegrity structure predicted by the CSD method is more accurate than that predicted by the Lagrangian method and the FEA method, especially in the high-frequency domain. This is supported by the dynamic responses predicted by the CSD method, which show the existence of the natural frequencies in the high-frequency domain, and the trend of convergence with more terms of member internal displacements being used. 4) The computational efficiency of the CSD method is verified, since accurate dynamic responses are predicted by the CSD method by using only a small number of internal terms of member displacements.

6. Conclusions

The Cartesian spatial discretization method is developed for nonlinear dynamic modeling and vibration analysis of tensegrity structures. Different from traditional dynamic modeling methods, which often oversimplify structural members of a tensegrity structure by neglecting internal displacements, this new method can accurately predict the dynamic response of a tensegrity structure by incorporating member internal displacements in the dynamic model so developed. In this method, the position of a structural member is defined as a summation of internal terms and boundary-induced terms in a global Cartesian coordinate system. A nonlinear dynamic model of the member is then derived from Lagrange's equations as a system of ordinary differential equations. This dynamic model can be linearized at an equilibrium configuration for vibration analysis. A dynamic model of the whole structure is finally assembled in a straight-forward way by using common nodal coordinates of structural members. The proposed method is applied to vibration analysis of a planar Snelson's X tensegrity structure, a three-dimensional tensegrity tower, and an irregular tensegrity grid, while compared with the Lagrangian method based on generalized coordinates, the commercial software ANSYS and the finite element analysis method, to show its capability to handle both simple and complex tensegrity structures. According to the simulation results, the proposed method can yield more natural frequencies and mode shapes with much higher accuracies than the Lagrangian method and the finite element analysis method, especially in the high-frequency domain. It is also demonstrated that the proposed method is computationally efficient as it converges in a super-linear rate by using only a small number of internal terms of member displacements.

Declaration of Competing Interest

The authors declare that they have no known competing financial interests or personal relationships that could have appeared to influence the work reported in this paper.

Data availability

Data will be made available on request.

Acknowledgement

The authors acknowledge support from the US NSF (National Science Foundation) through grant number 2104237.

Appendix A:. Derivation of equations of motion of the Snelson's X planar tensegrity structure by the Lagrangian method based on generalized coordinates

The derivation of equations of motion of the Snelson's X planar tensegrity structure shown in Fig. 4 by the Lagrangian method based on generalized coordinates is presented here. In this approach, the two bar members and the four cable members are treated as rigid bodies and massless linear elastic springs, respectively. The three generalized coordinates x_2, θ_1 and θ_2 are defined as the x-coordinate of node two, the angle between the first bar member and the positive x-direction and the angle between the second bar member and the positive x-direction, respectively (see Fig. 4). One can obtain the kinetic energies of the two bar members as

$$T_1 = \frac{1}{6} m_1 L_1^2 \dot{\theta}_1^2 \tag{A1}$$

$$T_2 = \frac{1}{6} m_2 (L_2^2 \dot{\theta}_2^2 - 3\sin\theta_2 L_2 \dot{\theta}_2 \dot{x}_2 + 3\dot{x}_2^2) \tag{A2}$$

where m_1 and m_2 are the masses of the two bar members, which can be calculated using the dimensional and material parameters given in Table 1, and L_1 and L_2 are the lengths of the two bar members, which can be calculated from the nodal positions. The potential energy of the four cable members can be calculated as

$$V_3 = \frac{E_3 A_3}{2L_3^0} (x_2 - L_3^0)^2 \tag{A3}$$

$$V_4 = \frac{E_4 A_4}{2L_4^0} \left(\sqrt{(L_1\cos\theta_1 - x_2)^2 + (L_1\sin\theta_1)^2} - L_4^0 \right)^2 \tag{A4}$$

$$V_5 = \frac{E_5 A_5}{2L_5^0} \left(\sqrt{(x_2 + L_2\cos\theta_2 - L_1\cos\theta_1)^2 + (L_2\sin\theta_2 - L_1\sin\theta_1)^2} - L_5^0 \right)^2 \tag{A5}$$

$$V_6 = \frac{E_6 A_6}{2L_6^0} \left(\sqrt{(x_2 + L_2\cos\theta_2)^2 + (L_2\sin\theta_2)^2} - L_6^0 \right)^2 \tag{A6}$$

where $E_i A_i$ is the longitudinal rigidity of cable member i, determined by the dimensional and material parameters given in Table 1, and L_i^0 is the undeformed length of cable member i, determined by the longitudinal rigidity ($E_i A_i$) and the tension force (100 N) of the member at the initial equilibrium configuration. Thus, the total kinetic energy and potential energy of the structure can be obtained as

$$T = T_1 + T_2 \tag{A7}$$

$$V = V_3 + V_4 + V_5 + V_6 \tag{A8}$$

Let the Lagrangian be $L^L = T\text{-}V$; the nonlinear equations of motion of the Snelson's X planar tensegrity structure can be derived using Lagrange's equations

$$\frac{d}{dt}\left(\frac{\partial L^L}{\partial \dot{q}}\right) - \frac{\partial L^L}{\partial q} = f_{nc} \tag{A9}$$

where $q = [x_2, \theta_1\ \theta_2]^T$, and f_{nc} is the non-conservative force. Values of some important parameters in Eq. (A.9) are given as: $m_1 = m_2 = 0.1944$ kg; $L_1 = L_2 = 1.4142\ m$; $E_3A_3 = E_4A_4 = E_5A_5 = E_6A_6 = 6.2832 \times 10^5 N$; and $L_3^0 = L_4^0 = L_4^0 = L_4^0 = 0.9998\ m$.

Equation (A.9) can be linearized at the equilibrium configuration $x_2 = 1\ m$, $\theta_1 = \pi/4$ and $\theta_1 = 3\pi/4$, for vibration analysis of the structure:

$$M\ddot{q} + Kq = f_{nc} \tag{A10}$$

where

$$M = \begin{bmatrix} 0.1944 & 0 & -0.0972 \\ 0 & 0.1296 & 0 \\ -0.0972 & 0 & 0.1296 \end{bmatrix}, \quad K = \begin{bmatrix} 1.2570 & 0.6285 & -0.6285 \\ 0.6285 & 1.2568 & -0.6283 \\ -0.6285 & -0.6283 & 1.2568 \end{bmatrix} \times 10^6 \tag{A11}$$

Appendix B:. Topology, nodal coordinates, material parameters and member internal forces of the three-dimensional tensegrity tower in Section 5.2

Nodal coordinates of the three-dimensional tensegrity tower in Section 5.2 are given in Table B1. The topology, material parameters, and member internal forces of the structure are shown in Table B2.

Table B1
Nodal coordinates of the three-dimensional tensegrity tower in Section 5.2 (m).

Node index	x	y	z
1	10.0000	0.0000	0.0000
2	−5.0000	8.6603	0.0000
3	−5.0000	−8.6603	0.0000
4	8.6603	5.0000	30.0000
5	−8.6603	5.0000	30.0000
6	−0.0000	−10.0000	30.0000
7	5.0000	8.6603	60.0000
8	−10.0000	0.0000	60.0000
9	5.0000	−8.6603	60.0000

Table B2
Topology, material parameters and member internal forces of the three-dimensional tensegrity tower in Section 5.2.

Member index	Nodes connected	Internal force (N)	Mass (kg)	Longitudinal rigidity EA (N)
1	(1, 5)	-1.0000×10^5	1.2454×10^6	1.8276×10^{10}
2	(2, 6)	-1.0000×10^5	1.2454×10^6	1.8276×10^{10}
3	(3, 4)	-1.0000×10^5	1.2454×10^6	1.8276×10^{10}
4	(5, 9)	-1.0000×10^5	1.2454×10^6	1.8276×10^{10}
5	(6, 7)	-1.0000×10^5	1.2454×10^6	1.8276×10^{10}
6	(4, 8)	-1.0000×10^5	1.2454×10^6	1.8276×10^{10}
7	(4, 5)	5.6051×10^4	62.3467	3.4816×10^7
8	(5, 6)	5.6051×10^4	62.3467	3.4816×10^7
9	(6, 4)	5.6051×10^4	62.3467	3.4816×10^7
10	(7, 8)	2.8025×10^4	31.1734	1.7408×10^7
11	(8, 9)	2.8025×10^4	31.1734	1.7408×10^7
12	(9, 7)	2.8025×10^4	31.1734	1.7408×10^7
13	(1, 4)	8.5318×10^4	166.8041	5.2996×10^7
14	(2, 5)	8.5318×10^4	166.8041	5.2996×10^7
15	(3, 6)	8.5318×10^4	166.8041	5.2996×10^7
16	(4, 7)	8.5318×10^4	166.8041	5.2996×10^7
17	(5, 8)	8.5318×10^4	166.8041	5.2996×10^7
18	(6, 9)	8.5318×10^4	166.8041	5.2996×10^7

References

Ali, N.B.H., Rhode-Barbarigos, L., Albi, A.A.P., Smith, I.F., 2010. Design optimization and dynamic analysis of a tensegrity-based footbridge. Engineering Structures 32, 3650–3659.

Ali, N.B.H., Smith, I., 2010. Dynamic behavior and vibration control of a tensegrity structure. International Journal of Solids and Structures 47, 1285–1296.

Ashwear, N., Eriksson, A., 2014. Natural frequencies describe the pre-stress in tensegrity structures. Computers & Structures 138, 162–171.

Ashwear, N., Tamadapu, G., Eriksson, A., 2016. Optimization of modular tensegrity structures for high stiffness and frequency separation requirements. International Journal of Solids and Structures 80, 297–309.

Barnes, M.R., 1999. Form finding and analysis of tension structures by dynamic relaxation. International journal of space structures 14, 89–104.

Caluwaerts, K., Despraz, J., Işçen, A., Sabelhaus, A.P., Bruce, J., Schrauwen, B., SunSpiral, V., 2014. Design and control of compliant tensegrity robots through simulation and hardware validation. Journal of the royal society interface 11, 20140520.

Cimmino, M., Miranda, R., Sicignano, E., Ferreira, A., Skelton, R., Fraternali, F., 2017. Composite solar façades and wind generators with tensegrity architecture. Composites Part B: Engineering 115, 275–281.

De Tommasi, D., Marano, G., Puglisi, G., Trentadue, F., 2017. Morphological optimization of tensegrity-type metamaterials. Composites Part B: Engineering 115, 182–187.

Faroughi, S., Lee, J., 2015. Analysis of tensegrity structures subject to dynamic loading using a Newmark approach. Journal of Building Engineering 2, 1–8.

Faroughi, S., Tur, J.M.M., 2015. Vibration properties in the design of tensegrity structure. Journal of Vibration and Control 21, 611–624.

Feng, X., 2017. The optimal initial self-stress design for tensegrity grid structures. Computers & Structures 193, 21–30.

Feng, X., Miah, M.S., Ou, Y., 2018. Dynamic behavior and vibration mitigation of a spatial tensegrity beam. Engineering Structures 171, 1007–1016.

Fergusson, N., Pilkey, W., 1993. Literature review of variants of the dynamic stiffness method, part 1: The dynamic element method. The Shock and vibration digest 25, 3–12.

Fuller, R.B., 1982. Synergetics: explorations in the geometry of thinking. Estate of R, Buckminster Fuller.

Furuya, H., 1992. Concept of deployable tensegrity structures in space application. International Journal of Space Structures 7, 143–151.

Ingber, D.E., 2003. Tensegrity I. Cell structure and hierarchical systems biology. Journal of cell science 116, 1157–1173.

Kahla, N.B., Ouni, M.H.E., Ali, N.B.H., Khan, R.A., 2020. Nonlinear dynamic response and stability analysis of a tensegrity bridge to selected cable rupture. Latin American Journal of Solids and Structures 17.

Kan, Z., Peng, H., Chen, B., Zhong, W., 2018a. Nonlinear dynamic and deployment analysis of clustered tensegrity structures using a positional formulation FEM. Composite Structures 187, 241–258.

Kan, Z., Peng, H., Chen, B., Zhong, W., 2018b. A sliding cable element of multibody dynamics with application to nonlinear dynamic deployment analysis of clustered tensegrity. International Journal of Solids and Structures 130, 61–79.

Lee, S., Gan, B.S., Lee, J., 2016. A fully automatic group selection for form-finding process of truncated tetrahedral tensegrity structures via a double-loop genetic algorithm. Composites Part B: Engineering 106, 308–315.

Liu, K., Zegard, T., Pratapa, P.P., Paulino, G.H., 2019. Unraveling tensegrity tessellations for metamaterials with tunable stiffness and bandgaps. Journal of the Mechanics and Physics of Solids 131, 147–166.

Ma, S., Chen, M., Skelton, R.E., 2022. Tensegrity system dynamics based on finite element method. Composite Structures 280, 114838.

Motro, R., 1996. Structural morphology of tensegrity systems. International Journal of Space Structures 11, 233–240.

Motro, R., Najari, S., Jouanna, P., 1987. Static and dynamic analysis of tensegrity systems. Computational Aspects. Springer, Shell and Spatial Structures, pp. 270–279.

Oppenheim, I.J., Williams, W.O., 2001a. Vibration and damping in three-bar tensegrity structure. Journal of Aerospace Engineering 14, 85–91.

Oppenheim, I.J., Williams, W.O., 2001b. Vibration of an elastic tensegrity structure. European Journal of Mechanics-A/Solids 20, 1023–1031.

Pellegrino, S., Calladine, C.R., 1986. Matrix analysis of statically and kinematically indeterminate frameworks. International Journal of Solids and Structures 22, 409–428.

Peng, H., Li, F., Kan, Z., 2020. A novel distributed model predictive control method based on a substructuring technique for smart tensegrity structure vibrations. Journal of Sound and Vibration 471, 115171.

Ren, H., Zhu, W., 2013. An accurate spatial discretization and substructure method with application to moving elevator cable-car systems—part II: application. Journal of Vibration and Acoustics 135.

Rhode-Barbarigos, L., Ali, N.B.H., Motro, R., Smith, I.F., 2010. Designing tensegrity modules for pedestrian bridges. Engineering Structures 32, 1158–1167.

Sarkar, A., Manohar, C., 1996. Dynamic stiffness matrix of a general cable element. Archive of applied mechanics 66, 315–325.

Schek, H.-J., 1974. The force density method for form finding and computation of general networks. Computer methods in applied mechanics and engineering 3, 115–134.

Shah, D.S., Booth, J.W., Baines, R.L., Wang, K., Vespignani, M., Bekris, K., Kramer-Bottiglio, R., 2021. Tensegrity robotics. Soft robotics.

Shekastehband, B., Abedi, K., Dianat, N., 2013. Experimental and numerical study on the self-stress design of tensegrity systems. Meccanica 48, 2367–2389.

Skelton, R.T., Sultan, C., 1997. Controllable tensegrity: a new class of smart structures, Smart structures and materials 1997: Mathematics and control in smart structures. International Society for Optics and Photonics 166–177.

Starossek, U., 1991. Dynamic stiffness matrix of sagging cable. Journal of engineering mechanics 117, 2815–2829.

Starossek, U., 1994. Cable dynamics-a review. Structural Engineering International 4, 171–176.

Sultan, C., Corless, M., Skelton, R.E., 2002b. Symmetrical reconfiguration of tensegrity structures. International Journal of Solids and Structures 39, 2215–2234.

Sultan, C., Skelton, R., 2003. Deployment of tensegrity structures. International Journal of Solids and Structures 40, 4637–4657.

Sultan, C., Corless, M., Skelton, R.E., 2002a. Linear dynamics of tensegrity structures. Engineering Structures 24, 671–685.

Tibert, A., Pellegrino, S., 2002. Deployable tensegrity reflectors for small satellites. Journal of Spacecraft and Rockets 39, 701–709.

Tran, H.C., Lee, J., 2010. Initial self-stress design of tensegrity grid structures. Computers & structures 88, 558–566.

Veuve, N., Safaei, S.D., Smith, I.F., 2015. Deployment of a tensegrity footbridge. Journal of Structural Engineering 141, 04015021.

Wu, K., Zhu, W., Fan, W., 2017. On a comparative study of an accurate spatial discretization method for one-dimensional continuous systems. Journal of Sound and Vibration 399, 257–284.

Yang, S., Sultan, C., 2016. Modeling of tensegrity-membrane systems. International Journal of Solids and Structures 82, 125–143.

Yang, S., Sultan, C., 2017. A comparative study on the dynamics of tensegrity-membrane systems based on multiple models. International Journal of Solids and Structures 113, 47–69.

Yang, S., Sultan, C., 2019. Deployment of foldable tensegrity-membrane systems via transition between tensegrity configurations and tensegrity-membrane configurations. International Journal of Solids and Structures 160, 103–119.

Yuan, S., Jing, W., Jiang, H., 2021. A Deployable Tensegrity Microrobot for Minimally Invasive Interventions, ASME International Mechanical Engineering Congress and Exposition. American Society of Mechanical Engineers, p. V005T005A061. https://doi.org/10.1115/IMECE2021-67009.

Yuan, S., Yang, B., 2019. The fixed nodal position method for form finding of high-precision lightweight truss structures. International journal of Solids and Structures 161, 82–95.

Yuan, S., Zhu, W., 2021. Optimal self-stress determination of tensegrity structures. Engineering Structures 238, 112003.

Zhang, J., Ohsaki, M., 2006. Adaptive force density method for form-finding problem of tensegrity structures. International Journal of Solids and Structures 43, 5658–5673.

Zhu, W., Ren, H., 2013. An accurate spatial discretization and substructure method with application to moving elevator cable-car systems—part I: methodology. Journal of Vibration and Acoustics 135.